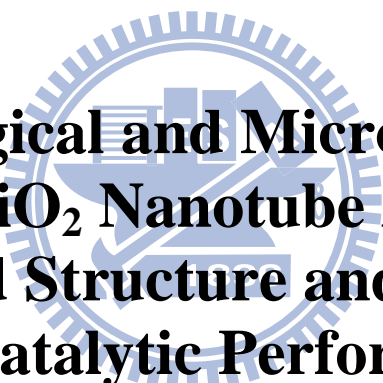# 國立交通大學
材料科學與工程學系
博士論文

二氧化鈦奈米管陣列與複合結構之形貌
與結構特性及其光催化性質之研究

Morphological and Microstructural Study on TiO$_2$ Nanotube Arrays and Hybrid Structure and Their Photocatalytic Performance

研究生：徐明義

指導教授：呂志鵬博士

中華民國一百零一年五月

二氧化鈦奈米管陣列與複合結構之形貌與結構特性及其光催化性質之研究

Morphological and Microstructural Study on TiO₂ Nanotube Arrays and Hybrid Structure and Their Photocatalytic Performance

研 究 生：徐 明 義 Student：Ming-Yi Hsu

指導教授：呂 志 鵬 博士 Advisor：Dr. Jihperng Leu

國 立 交 通 大 學

材 料 科 學 與 工 程 學 系

博 士 論 文

A Thesis

Submitted to Department of Materials Science and Engineering

College of Engineering, National Chiao Tung University

in partial Fulfillment of the Requirements

for the Degree of Doctor of Philosophy

May 2012

Hsinchu, Taiwan, Republic of China

中 華 民 國 一 百 零 一 年 五 月

二氧化鈦奈米管陣列與複合結構之形貌與結構特性及其光催化性質之研究

研究生: 徐明義　　　　　　　　　　　　　　指導教授: 呂志鵬 博士

國立交通大學材料科學與工程學系 博士班

摘要

本研究針對使用陽極處理法製備二氧化鈦奈米管陣列(TiO$_2$ nanotubes arrays, TNAs)與其奈米線複合結構(TNWs/TNAs)之製程參數與後熱處理方法進行一連串的顯微結構分析與形貌演進之探討。首先，以兩種不同氟化物:氫氟酸(Hydrogen fluoride, HF)與氟化銨(Ammonium fluoride, NH$_4$F) 製備 TNAs 後，進行不同溫度之後熱處理，再以 X-光粉末繞射儀(XRD)、掃瞄式電子顯微鏡(SEM)和 X 光近緣結構(XANES)進行分析討論。其結果顯示以 HF 製備出 TNAs 含 90% 非晶相(amorphous)與 10% Ti^{2+} (TiO) 與 Ti^{3+} (Ti$_2$O$_3$)之低氧量鈦化物。而經過 400°C 熱處理之後，其結構轉變成 93%銳鈦礦相(anatase)、6% 非晶相與 1% 低氧鈦化物。相反地，以 NH$_4$F 製備出 TNAs 則是含較低之非晶相 TiO$_2$(82%)與較高的低氧鈦化物(18%)，其原因乃是由於電解質中只有少量的 1 wt% 水添加量，使得溶液中氧離子供應量不足而產生較多低氧鈦化物。經過 400°C 熱處理之後，其二氧化鈦奈米管之結晶度只增加至 86%銳鈦礦相。此低結晶度可推論是因為 NH$_4$ 解離之 NH$_4^+$與 TiF$_6^{2-}$ 反應形成(NH$_4$)$_2$TiF$_6$ 化合物所致。

另一方面，本研究利用準分子雷射以垂直式(parallel mode)與旋轉式(tilted mode)兩種方法來進行在二氧化鈦後熱處理。其研究結果發現垂直式照射試片表面之後熱處理只能達到相較 400°C 1h 後熱處理之 50%結晶度。因為垂直式後熱處理使得一維二氧化鈦奈米管的熱傳遞方向只能從表面開始向下產生相變化，再

加上過薄的滲透深度與太短的脈衝持續時間(25 ns)，而限制了材料之結晶度。然而，若使用旋轉式，當角度旋轉至與雷射源呈 85° 時，其結晶度可達相較 400°C 1h 後熱處理 90%之結晶度。推測因為旋轉式增加了雷射照射的面積以及較佳的雙向熱傳導方式為其主要原因。

此外，本研究亦順利以乙二醇(ethylene glycol)與 NH_4F 之含水電解質在無攪拌環境中以一階段方式製備出二氧化鈦奈米線直接連接奈米管之複合結構(TNWs/TNAs)，實驗中利用改變電壓與時間所得之結構形貌來推論其複合結構形成機制包含以下四個步驟: (1) 在未攪拌系統中產生管壁厚度不均勻的 TNAs，其管口部分受到蝕刻使得管壁漸漸變薄，(2) 較薄的管壁開始被蝕刻出小洞，且小洞開始連結，(3) 連結的小洞將 TNAs 漸漸分開成奈米線，最後(4) 奈米線的尺寸也受到蝕刻而隨著時間越來越細。除此之外，在光催化性質之分析結果發現: 由於較高之比表面積與電子傳輸特性，二氧化鈦奈米線/奈米管之結構相較二氧化鈦奈米管對具有較佳之光催化特性，而且 20 nm TNWs/40 nm TNAs 可達到與二氧化鈦奈米粉末相接近光觸媒特性。

Morphological and Microstructural Study on TiO$_2$ Nanotube Arrays and Hybrid Structure and Their Photocatalytic Performance
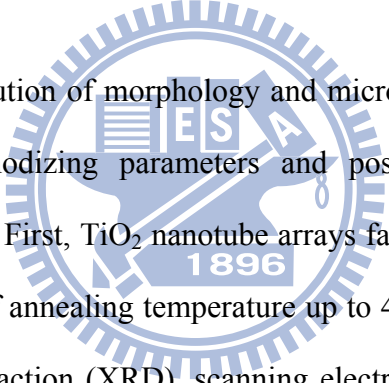
Student: Ming-Yi Hsu   Advisor: Dr. Jihperng Leu

Department of Materials Science and Engineering

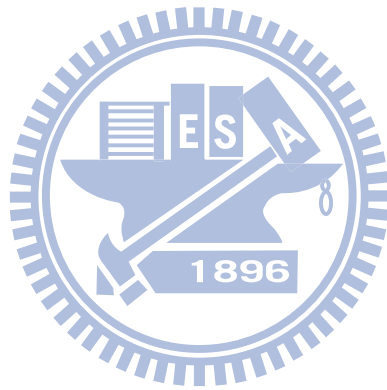National Chiao Tung University

Abstract

In this study, the evolution of morphology and microstructure of anodized TiO$_2$ films by changing the anodizing parameters and post annealing process were investigated and compared. First, TiO$_2$ nanotube arrays fabricated with HF and NH$_4$F electrolytes as a function of annealing temperature up to 400 ^{o}C was investigated and compared using x-ray diffraction (XRD), scanning electron microscopy (SEM), and x-ray absorption near-edge structure spectroscopy (XANES). Results showed that TiO$_2$ nanotube arrays grown in HF electrolyte contained 90% amorphous TiO$_2$ and 10% lower oxidation states of titanium from Ti^{2+} (TiO) and Ti^{3+} (Ti$_2$O$_3$) cations. After annealing at 400°C, TiO$_2$ nanotube arrays underwent charge transfer and phase transformation to 93% anatase phase, 6% amorphous TiO$_2$, and 1% suboxides. In contrast, as-grown TiO$_2$ nanotube arrays using NH$_4$F electrolyte possessed less amorphous TiO$_2$ (82%) but more suboxides (18%) due to lower oxygen ion formation from scanty 1wt% H$_2$O addition. Moreover, when annealed to 400°C, the crystallinity of TiO$_2$ nanotube arrays increased only to 86% for the anatase phase. The lower

anatase phase could be attributed to the formation of $(NH_4)_2TiF_6$ type compounds presumably formed by the reaction of TiF_6^{2-} and NH_4^+ ions dissociated from NH_4F.

On the other hand, for TNA post annealing technology, the excimer laser annealing (ELA) were investigated as a function of the laser fluence using parallel and tilted modes. Results showed that the crystallinity of the ELA-treated TNAs reached only about 50% relative to that of TNAs treated by furnace anneal at 400^oC for 1 hr. The phase transformation starts from the top surface of the TNAs with surface damage resulting from short penetration depth and limited one-dimensional heat transport from the surface to the bottom under extremely short pulse duration (25 ns) of the excimer laser. When a tilted mode was used, the crystallinity of TNAs treated by ELA at 85° was increased to 90% relative to that by the furnace anneal. This can be attributed to the increased area of the laser energy interaction zone and better heat conduction to both ends of the TNAs.

Furthermore, TiO_2 nanowires connected directly with TiO_2 nanotubes arrays (TNWs/TNAs) were successfully fabricated with a mixture of ethylene glycol and water that contained NH_4F electrolyte via a one-step method without mechanical stirring. The morphology of the TNWs/TNAs structure was investigated by changing the anodizing voltage and processing time to elucidate its formation mechanism. Well-developed anodic oxide nanowires are only observed under specific anodizing voltage and processing time conditions. The evolution of TNWs follows four stages: (1) thinning of the tube wall thickness with high roughness near the TNA mouths, (2) forming strings of through holes in the upper section of the TNAs, (3) splitting into nanowires, and (4) collapsing and further thinning of nanowires. For photocatalytic application, TNWs/TNAs film demonstrated a better photocatalytic performance than regular TNAs due to higher surface area and improved charge transport. Moreover,

TNWs/TNAs film (20 nm wire/40 nm pore diameter) achieved a performance comparable to that of the film made from TiO_2 nanoparticles.

Acknowledgement

Contents

Table Captions

Figure Captions

XI

Explanation of abbreviations and Symbols

I	Absorption intensity
E_g	Band gap enegy
C	Concentration
ρ	Density
E	Electric field strength
τ	Pulse duration time
R	Reflectivity
Cp	Specific heat
k	Thermal conductivity
L_T	Thermal diffusion length
D_{th}	Thermal diffusivity
λ	Wavelength
DSSC(s)	Dye sensitized solar cell(s)
EG	Ethylene glycol
ELA	Excimer laser annealing
FIB/SEM	Focused ion beam scanning electron microscope
HRTEM	High resolution transmission electron microscopy
LFS	Ligand-field splitting
MB	Methylene blue
1D	One dimensional
FESEM	Scanning electron microscopy
SAD	Selected area diffraction
TNA(s)	TiO_2 nanotube arrays
TNW(s)	TiO_2 nanowires
TiO_2	Titanium dioxide
TEM	Transmission electron microscopy
XANES	X-ray absorption near-edge structure spectroscopy
XRD	X-ray diffractometer

Chapter 1 Introduction

1.1 Background

Since the first report on electrochemical photolysis of water at titanium dioxide (TiO_2) electrodes by Fujishima and Honda [1], enormous efforts have been devoted to the research of TiO_2 material, which has led to many promising applications in areas ranging from electrochromic [2,3], photocatalytic devices [4,5,6], sensors [7,8], and solar cells [9,10,11]. The applications of TiO_2 are primarily determined by its properties such as crystalline structure, specific surface area, particle size, porosity, and thermal stability. TiO_2 can exist in anatase, rutile or brookite crystalline phase [12], in addition to amorphous phase. For photocatalytic application, the anatase phase is more active than the rutile phase, due to its larger band gap and lower electron-hole recombination probability [13]. Also, increased degree of anatase phase in crystalline TiO_2 was found to enhance the catalytic activity, for example, in the photocatalytic degradation of organic pollutants [14,15]. Such enhancement of photocatalytic activity could be attributed to the reduction of amorphous domains, defects, or impurities, which acted as the recombination centers for photogenerated electrons and holes [16,17]. For dye sensitized solar cells (DSSCs) application, it was also found that electron transport was slower in rutile phase than in anatase phase due to their difference in the extent of interparticle connectivity associated with the TiO_2 particle packing density [18].

In addition, in order to conform to flexible devices regulations, low-temperature processing is an important factor. But, in TiO_2 fabrication, to increase the crystallinity of TiO_2 structure after formation, post annealing is typically required to change its structure from amorphous to anatase phase. Nevertheless, thermal annealing treatment using a conventional high temperature furnace annealing takes hours to complete the

transformation of the crystal structure of the film. To expedite the annealing time or deliver low-temperature processing for flexible devices using polymer substrates with low glass transition temperature and poor thermal stability, excimer laser annealing (ELA) is one of the preferred fast processing technologies [19,20]. It has been reported that the phase transition from amorphous to anatase or rutile phase is observed within a nanosecond time scale by laser treatment [21,22]. So far, most studies have been carried out on TiO_2 powders [22] or thin films [23]. However, only a small depth of material is processed upon ELA irradiation because most extreme heating of pulsed laser annealing is confined to the near-surface region of the sample due to the short duration of the UV laser pulse. The challenge is to overcome the limited penetration depth in thick TNAs.

In addition to the microstructure, the electron transport is another critical property influencing TiO_2 applications such as DSSCs [24]. In recent years, various forms of TiO_2 nanostructure such as nanorods, nanowires, and nanotubes have attracted significant research interests in hope to achieve higher charge carrier transport than the nanoparticles [25 , 26]. Several studies reported that one dimensional (1D) nansostructures could improve the charge-collection efficiency by promoting faster transport and slower recombination due to its axial transport path as compared to the random transport path in nanoparticles [9,27]. TiO_2 nanotube arrays (TNAs) grown by electrochemical anodization method was first reported by Zwilling et al. [28] with a length up to 500 nm (10:1 aspect ratio) using HF-based aqueous electrolyte. Moreover, several neutral electrolytes have been employed to prepare anodized TiO_2 nanotubes with higher aspect ratio [29,30]. In specific, high aspect ratio (100:1), self-organized TiO_2 nanotubes could be obtained from ethylene glycol (EG) solution [30]. However, most of studies are dedicated to one specific type of 1D TiO_2 structures with less research on 1D TiO_2 hybrid structures. Recently, Lim and Choi [31] demonstrated the

TiO$_2$ nanowires directly connected TiO$_2$ nanotubes arrays structure (designated as TNWs/TNAs) using EG and NH$_4$F under mechanical stirring and proposed a bamboo-splitting model. Moreover, Wang et al. [32] used a TNWs/TNAs hybrid structure, prepared by anodization and hydrothermal two-step method, for dye-sensitized solar cells application. The DSSCs with such TiO$_2$ hybrid structure exhibited higher photovoltaic parameters and a lower dark current [32]. Yet, the details of the formation mechanism for TNWs/TNAs still need to be clarified. Also, little work has been reported on the applications of TNWs/TNAs and TNAs for their photocatalytic properties.

1.2 Objectives of the thesis

Based on the above description, there are still some weaknesses and controversies to be resolved and the primary aim of this thesis is to investigate some of them and to provide new insights on the subject. First, we are interested in the microstructures and composition of TiO$_2$ nanotube arrays as prepared by anodic oxidation in HF and NH$_4$F electrolytes. In addition to conventional X-ray diffraction (XRD), X-ray absorption near-edge structure spectroscopy (XANES) was employed to probe element-specific partial density of empty electronic states in different polymorphs of TiO$_2$ and any lower oxidation states such as TiO and Ti$_2$O$_3$ [33,34,35]. Furthermore, the evolution of microstructure and suboxides (TiO and Ti$_2$O$_3$) in the TiO$_2$ nanotubes prepared by HF and NH$_4$F electrolytes as a function of annealing temperature was investigated and compared. The mechanism responsible for their difference in XANES spectra of different amount of crystalline, amorphous phases and lower oxidation states of titanium in TiO$_2$ nanotube arrays will be proposed.

Also, excimer laser annealing treatment on TNAs has been optimized for the production of crystalline structure. The evolution of morphology and microstructure in TNAs were investigated as functions of laser fluence. The mechanisms of phase transition and the changes of the surface of TNAs induced by laser are proposed. Furthermore, laser annealing in a tilted mode has been developed to resolve the limited penetration depth in a parallel mode. Its difference in the structural and morphological transformation of TNAs will be examined and discussed.

Furthermore, this study proposes a one-step method for the fabrication of a TNWs-covered TNAs hybrid structure, using a mixture of EG and water containing NH_4F electrolyte without mechanical stirring. The morphology of the TNWs/TNAs structure was then examined by changing the anodizing voltage and processing time, to elucidate the detailed formation mechanism of TNWs/TNAs. The photocatalytic degradation of methylene blue (MB) using various TNWs/TNAs and TNAs structures was investigated and compared with the film made of TiO_2 nanoparticles.

1.3 Overview

The goal of this thesis is to study the structural and morphological transformation of TNAs and TiO_2 hybrid structure using electrochemical anodization techniques, and furthermore approach some photocatalytic applications of these materials. The important electrochemical parameters controlling the growth of the hybrid structure have been extensively studied and optimized. Also, appropriate post-fabrication processing conditions such as heat treatment conditions have been optimized for the high crystallinity TiO_2. Chapter 2 offers a literature survey on the TiO_2 materials, development of fabrication methods for TiO_2 nanotubes, and annealing method for TiO_2 crystallization. Chapter 3 covers the experimental method and instrumentation.

Chapter 4 discusses the microstructure and composition of TiO_2 nanotube arrays fabricated with HF and NH_4F electrolytes and their evolution during annealing. Chapter 5 discusses the structural and morphological transformation of TiO_2 induced by excimer laser annealing. Chapter 6 describes the formation mechanism of TiO_2 hybrid structure (TNWs/TNAs), and presents the photocatalysis applications. Finally, Chapter 7 provides a summary of the key results in this study.

Chapter 2

Literature Review

This chapter is a review of journals and references available in literature that are relevant to the research topic. Section 2.1 is an introduction of TiO_2 materials. Section 2.2 is synthesis of TiO_2 nanostructure, and section 2.3 is a discussion on anodic oxidization technique. Finally, the annealing method for TNAs crystallization is described in section 2.4.

2.1 Introduction of TiO_2 materials

Titanium dioxide (TiO_2) is the most commonly used compound of titanium. Since its commercial production in the early twentieth century, TiO_2 has been widely used as a pigment in sunscreens, paints, ointments, and toothpaste. TiO_2 powder is chemically inert, stable under sunlight, and is very opaque: This allows it to impart a pure and brilliant white color to the brown or gray chemicals that form the majority of household plastics. However, in 1972, Fujishima and Honda discovered the phenomenon of photocatalytic splitting of water on a TiO_2 electrode under ultraviolet (UV) light. Since then, enormous efforts have been devoted to the research of TiO_2 [36].

TiO_2 can exist in three distinct crystalline polymorphs: anatase, rutile, or brookite crystalline phase, respectively shown in Fig. 2.1 [37]. From Fig. 2.1, all three crystal structures are made up of distorted octahedra, each one representing a TiO_6 unit, where each Ti^{4+} is at the centre of the unit and coordinates six O^{2-} ions. The manner in which the octahedra assemble to form a TiO_6 based chain is different and characteristic of each polymorph. In these three phases, rutile and anatase are the most commonly synthesized phases. Anatase and brookite are metastable phases and convert into rutile at high

6

temperature, usually above 600 °C [38]. Table 2.1 lists some of the key properties [37,39] of the three TiO_2 polymorphs. Both rutile and anatase have a tetragonal crystal structure, whereas brookite has an orthorhombic symmetry. Rutile is the densest phase and has the highest refractive index, while anatase is characterised by the widest band-gap (~3.2eV) [39]. The properties (density, band-gap and refractive index) of brookite fall between those of rutile and anatase.

2.2 Synthesis of TiO_2 nanostructure

The wide ranging properties of TiO_2 have generated a great deal of interest in many different fields. Many researchers have focused their studies on the production and processing of nanostructure TiO_2. One of the most obvious advantages provided by nano-materials is that of the greatly increased surface area offered by small nanoparticles. For example, in DSSCs applications, the active electrode in the DSSC is composed of a high surface area TiO_2 nanoparticle film that carries an anchored organic dye [2]. However, as the injected electrons, which excited from dye, diffuse through the TiO_2 particle network to the collecting transparent conducting oxide (TCO) substrate, due to the randomly packed TiO_2 nanoparticle (NP) films, it has been inferred that transport is limited by the residence time of electrons in traps. In recent years, in order to reduce random-walk effects and suppress potential recombination at grain boundaries, 1D morphologies such as nanowires, nanorods and nanotubes have been explored as an alternative to nanoparticle based films. Thus, various approaches such as template synthesis [40,41,42], chemical vapor deposition (CVD) [43], hydrothermal reactions [44,45], and anodic oxidization [28, 46 , 47 , 48] have been developed for preparing TiO_2 nanostructure. Among these approaches, anodic oxidization is a relatively low cost process and represents a simple technique that can be easily automated for preparing TiO_2

nanostructure. The following part of the chapter reviews the most relevant achievements regarding the research on anodic oxidization TiO_2 nanotubes, along with a discussion of current ideas and understanding of the process.

2.3 Anodic oxidization technique

2.3.1 The developments of anodized TiO_2 nanotubes

First generation of TiO_2 nanotubes

In 1999, Zwilling and co-workers anodized Ti and Ti–6Al–4V(TA6V) alloy in an electrolyte containing 0.5 mol/l chromic acid and 0.095 mol/l HF [28], while the first report on anodized TiO_2 nanotubes (called first generation). A typical porous structure obtained in TA6V is shown in Fig. 2.3. It was clear that the nanoporous structure observed only formed when sufficient HF was added to the electrolyte mixture, as pure chromic acid (CA) was leading to the formation of a thin but stable oxide layer with no apparent pore structure. However, unlike anodized alumina, where tube length increases indefinitely with anodizing time, TiO_2 nanotubes reach a steady state length when anodized. That is, after typically 10 to 20 minutes of anodization, the etching rate equals the dissolution rate so that the tube length does not show any further increase with additional anodizing time [28].

Second generation of TiO_2 nanotubes

In subsequent work, Grimes and co-workers overcome this limitation since they used other fluorine salts (as fluorine ion source besides HF) and combined buffers, bases and milder acids to adjust the pH and fluorine ion content. Salts like KF, NH4F or NaF totally dissociate in aqueous solution and then hydrolyze with water to form HF [49,50]. Moreover, HF is a relatively mild acid and in acidic solutions (pH<3.45) more than 50%

of the fluorine exists in the form of HF. As a result pH and fluorine ion concentration are closely related (and solutions with KF, NaF or NH$_4$F and no additional acid are basic.) The experiment worked found that they could grow nanotubes up to 4.4 μm (Fig. 2.4) using a solution of 0.1M KF as fluorine source, 1M H$_2$SO$_4$ as acid, 0.2 M citric acid presumably serving as buffer and NaOH as base to be added until the desired pH of 4.5 was obtained [50]. Later in 2005 Grimes and coworkers reported even longer nanotubes of up to 6 μm, over 17 to 20 h of anodization using the same electrolyte as before [51,52].

Third generation of TiO$_2$ nanotubes

The third generation of nanotubes refers to smooth tubes (i.e. no ripples along the wall), prepared in organic electrolytes (some almost water-free), where the dissolution rate of the forming oxide is minimized. For clarity a comparison of SEM cross section images, taken from literature [30], of nanotubes grown respectively in an aqueous and in an organic environment are shown, respectively, in Fig.2.5. It can be observed that tubes obtained in water are much rougher an irregular (i.e. ripples along the wall) than the smooth tubes grown in organic solution. The reason was to use a viscous electrolyte, where ion diffusion is slower than in water, to increase the pH gradient between the bottom and the top of the tubes. This led to the formation of TiO$_2$ nanotubes up to 7 μm thick (compared to 0.5 μm for first generation). They also attributed the smoothness and the regular morphology of the tube walls to the lower diffusion coefficient of the electrolyte which suppresses pH bursts at the pore bottom which occur when working in aqueous media. Over the last few years, TiO$_2$ nanotube arrays with lengths of up to approximately 1000 μm were achieved using a non-aqueous, polar organic electrolyte such as formamide, dimethyl sulfoxide, ethylene glycol or diethylene glycol [53,54,55]. In 2007, Grimes and co-workers published the synthesis of 0.36 mm long nanotubes [53],

practically demonstrating that the nanotube lengths was only limited by the initial titanium foil thickness. The following section will discuss the fundamental aspects and chemistry of the growth of TiO$_2$ nanotubes by anodization.

2.3.2 The growth of TiO$_2$ nanotubes: fundamental aspects

Formation mechanism of TiO$_2$ nanotube arrays

The formation mechanism of TNAs structures is similar to anodic aluminum oxide (AAO), which is the result of competition between field-assisted anodic oxidation, defined as the formation of the anodic layer under an applied electric field by Eqs. (2.1)-(2.3) and chemical/field assisted dissolution of the forming oxide by Eq. (2.4), which can be regarded as dissolution promoted by the presence of fluoride ions (chemical dissolution) and by the electric field weakening the bond between Ti and O (field assisted dissolution) [56] :
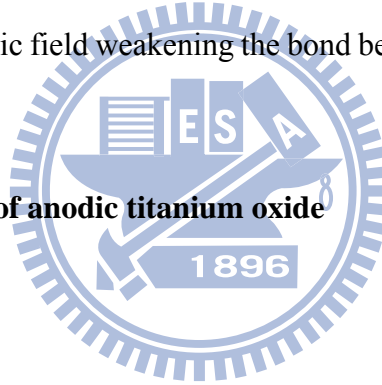
Electrochemical reactions of anodic titanium oxide
At Ti/Ti oxide interface:

$$Ti \rightarrow Ti^{2+} + 2e^{-} \tag{2.1}$$

$$2H_2O \rightarrow 2O^{2-} + 4H^{+} \tag{2.2}$$

$$Ti^{2+} + 2O^{2-} \rightarrow TiO_2 + 2e^{-} \tag{2.3}$$

At TiO$_2$/solution interface:

$$TiO_2 + 6HF \rightarrow TiF_6^{2-} + 2H_2O + 2H^{+} \tag{2.4}$$

Meanwhile, the formation mechanism of the TiO$_2$ nanotubes at various stages is schematically illustrated by Figs. 2.6(a)-(d). Initially, field-enhanced oxidation occurs at the Ti/Ti oxide interface by Eqs. (2.5)-(2.7) when oxygen ions diffusion to the Ti layer as shown in Figs. 2.6(a). At the same time, competing field-enhanced oxide dissolution occurs at TiO$_2$/solution interface illustrated by Fig. 2.6(b). Specifically, fluoride-containing electrolyte reacts with TiO$_2$ to form TiF$_6$$^{2-}$ as described by Eqs. (2.4). Moreover, small pores are generated and spread uniformly over the surface of the film under an electric field. When the pore to pore distance achieves a suitable value at

which the electric field of each pore would not affect to each other, the distribution of electric-field strength would change. As a consequent, increased in local field strength at the bottom of the pore in conjunction with low dissolution rate at sidewall, highly-order pore structures were formed as shown by Fig. 2.6(c). Finally, in the growth stage, fully developed TiO_2 nanotube arrays are shown in Fig. 2.6(d). Field-enhanced dissolution developed the depth of pore and, therefore, the steady-state nanotubes morphology was created.

Key parameters for controlling the growth of the nanotubes

Summarizing these observations, the key parameters to be taken into account when growing anodized TiO_2 nanotubes are the following:

Electrolyte

The electrolyte plays a crucial role in the growth of anodized TiO_2 nanotubes, as previously discussed. The main distinction is between aqueous and organic-based, where the water content is the important rule to limit dissolution of the oxide. Moreover, the pH of the solution is also important, considering the higher dissolution rate of the oxide in an acidic environment. As shown schematically in Fig. 2.7. While the pore bottom is at a low pH, the pore mouth (top of the pores/tubes) remains under a protective environment (higher pH) by using chemical buffer species $[NH_4F/(NH_4)_2SO_4]$. The rapid rate of TiO_2 dissolution in the first generation of nanotubes was reduced by replacing the HF acid with less aggressive solutions containing fluoride salts, raising the maximum thickness up to 2-3μm [29]. This is one of the reasons why dissolution of the anodic oxide is at its lowest when using fluoride salts (some of them have basic hydrolysis) instead of hydrofluoric acid.

Mechanical stirring system

The mechanical stirring was sometimes used to accelerate the reaction rate for nanotube growth. In addition, mechanical stirring also affect the inner tube morphology of TNAs. Fig. 2.8 shows the schematic diagram of the formation of tube spatial periodicity under different conditions: (a) without stirring; (b) at medium stirring rate; (c) at high stirring rate [57]. The smoothing effect of the tube inner surface and the acceleration of the growth are due to the redistribution of the F^- anions in the nanotubes. Based on the experimental results, the mechanism has been discussed with the consideration of the local reactions and transport processes of the main reaction species. Under this interpretation, the current oscillation and the morphology change in the pore are attributed to the redistribution of the ionic species by the fluctuation in the tube layer when there is no stirring. They can be significantly influenced by the convection above the tube layer and the slow transport process in the tubes with the existence of mechanical stirring.

Temperature

The temperature of the electrolyte affects the chemical dissolution and electrochemical etching rate in the growth of nanotube arrays via anodic oxidation of titanium. For example Grimes reported nanotube arrays were grown with a constant 10 V anode potential in an electrolyte of acetic acid plus 0.5% HF mixed in 1:7 ratio and kept at each of four different electrolyte bath temperatures: 5°C, 25°C, 35°C and 50°C. Table 2.2 shows the variation in 10 V wall thicknesses and tube length as a function of anodization temperature. Results show that with decreasing anodization bath temperature, the length of the nanotubes increases from 120 nm at 50°C to 224 nm at 5°C. Also, with decreasing anodization temperature the wall thickness increases from 9 nm at 50°C to 34 nm at 5°C, confirming the trend of increasing nanotube wall thickness

with lower anodization temperature [58].

2.3.3 Applications of TiO$_2$ nanotubes arrays

The main motivation behind research on anodized TiO$_2$ nanotubes is the possibility to investigate their impact on a wide range of technologies, including photocatalysis [59,60], chemical sensing [61,62,63] and photovoltaic devices such as DSSCs [64]. As a result, these applications are described in detail in the following sections.

Photocatalysis

Since the pioneering work by Honda and Fujishima [1], photocatalysis using various semiconductors has received much attention for their potential in the utilization of light energy. In particular, TiO$_2$ photocatalysts have been extensively studied due to relative cheap, high chemical stability and high reactivity of photo-generated holes. Most work on TiO$_2$ photocatalysts has been devoted to the study of reactions associated with the photodecomposition of H$_2$O into H$_2$ and O$_2$. The principle of the photocatalysis is shown in Fig. 2.9. According to this simplified scheme, electron-hole pair generated upon UV excitation is trapped at the surface as spatially separated redox centers. The reactive electron reduces O$_2$ from air initially to a superoxide and finally to hydrogen peroxide and an OH radical, whereas the reactive hole oxidizes the pollutant to its radical cation either directly or through a primarily formed OH radical produced by the oxidation of ubiquitous water. Thus, both the reductive and oxidative interfacial electron transfer processes lead to strong oxidizing agents which can induce mineralization of organic and inorganic pollutants and kill bacteria.

It has been known that TiO$_2$ with high surface area and crystallinity can enhance catalytic abilities [65,66,67], because high surface area increases the adsorption of reactants more efficiently and crystallinity decreases the electron-hole recombination

13

sites. Therefore, many efforts have been directed to create high surface area structure with crystallinity, nanostructured TiO_2. TiO_2 nanotubes have been also studied for dehydrogenation of ethanol [59], decomposition of gaseous isopropanol into acetone and carbon dioxide [60].

Chemical sensing

Semiconducting metal-oxides such as ZnO, SnO2 and TiO2 have been widely utilized for applications in gas sensors. Their gas sensing properties are largely based on the surface reaction between the metal-oxides and adsorbed gas species. The charge transfer interactions on the surface of such metal oxides, i.e., the adsorption of negatively charged oxygen and the oxidative/reductive interaction between target gases and adsorbed oxygen, lead to the significant variation in electrical conductivity upon exposure to analyte gases.

To meet the requirements of environmental and air-quality monitoring, there have been significant efforts to enhance the sensitivity of gas sensors. Recently, many nano technological approaches have been employed to enlarge the surface area or improve the charge-collection efficiency. From this perspective, sensing materials with one-dimensional (1D) geometry are very promising for their high sensitivity and fast response speed. Thus far, various promising 1D materials such as carbon nanotubes and Si nanowires have been studied for the fabrication of high sensitivity chemical sensors. For example, Comini et al. [61] used nanobelts for CO and NO2 sensing. The nanobelt sensors detected a few ppb levels of NO_2, which was difficult to monitor with conventional sensors. Vargese et al. [62] used TiO_2 nanotubes for high sensitivity sensors and the sensitivity of nanotube sensors reached up to 10^3. Ryu et al. [63] created TiO2 nano-honeycomb structure by using photoelectron chemical etching and applied it as a H_2

sensor. They reported that the nano-honeycomb structure enhanced the response time as well as the sensitivity.

Dye-Sensitized Solar Cells (DSSC)

Dye-sensitized solar cell (DSSC) is low cost alternative to inorganic semiconductor photovoltaic devices. Energy conversion in a DSSC is based on the injection of an electron from a photo-excited state of the sensitizer dye (typically a bipyridine metal complex) into the conduction band of semiconductor (TiO_2 is by far the most employed semiconductor). The original state of the dye is subsequently restored by electron donation from the electrolyte, usually an iodide/triiodide redox couple system. The iodide is regenerated at the counter electrode by electrons passed through a load.

The large band gap semiconductor, TiO_2, in DSSC is usually fabricated in the form of nanoporous structure in order to increase the contact of dye-TiO2 and simultaneously allow dye to directly contact with the redox electrolyte. Also, light absorption at the dye on nanoporous TiO_2 is higher than that on flat TiO2 surface which only harvests a negligibly small fraction of the incoming light [68].

Lately, research has been directed toward synthesizing structures with a high degree of order than the random assembly of nanoparticles. A desirable morphology of the films would have the mesoporous channels or nanorods aligned parallel to each other and vertically with respect to the glass substrate. This would facilitate charge diffusion in the pores and the mesoporous film, giving easier access to the film surface, avoiding grain boundaries and allowing the junction to be formed under better control. One approach to fabricate such oxide structures is based on anodized TiO_2 nanotubes by by Frank and co-workers [64]. They reported that the nanotubes and the nanoparticles in conventional DSSCs have similar transport properties (i.e. the electron has to diffuse

15

through the oxide and reach the electrode to feed the circuit), however lower recombination occurs in the nanotubes because of a higher charge collection efficiency. In addition, the nanotubes harvest the light more efficiently than conventional DSSCs, because of stronger light scattering effects, however their use in DSSCs is far from optimized.

2.3.4 Challenges of TiO$_2$ nanotubes arrays

From the literature, it has know crystalline nanotube or nanowire based TiO2 , in contrast with the random transport path in nanoparticle, have been investigated to improve electron collection. But, there still have challenges need to overcome. One key challenge of using vertically aligned 1-D nanostructures is that, compared to mesoporous films, the 1-D nanostructures typically have a low internal surface area. For example, in DSSC application, the reported efficiency of TiO2 NT based DSSC is generally much lower than that of DSSCs based on nanoparticles and amounted to 0.61%–2.9% [10,11,27,69]. The possible reason is that the internal surface area of NT based photoanode is much smaller than that of NPs, with a lower dye loading and sunlight absorption.

It seems that the high surface area and the good electron transport cannot be satisfied simultaneously in DSSC based on simple TiO$_2$ nanostructures of first generation. In order to satisfy both requirements we should design more complex nanostructures with a multiscale organization, in which small nanoparticles, nanowires or nanotubes are organized around long central cores connected directly to the electrode. This is a next generation of TiO$_2$ nanostructures that has a great potential to simultaneously provide high surface area and good electron transport properties.

2.4 Annealing of the nanotubes

Factors such as crystal structure, degree of crystallinity of the anodized TiO_2 nanotubes have to be taken into account in order to optimize their use in any possible application. For example the crystal structure is very important in photovoltaic applications, since it affects the ability to separate and transport charges (i.e. therefore affecting the performance of the device). However, As-prepared anodized TNAs are usually reported to be amorphous phase. To increase the crystallinity, post annealing is required to change its structure.

Nevertheless, thermal annealing treatment using a conventional furnace annealing takes hours and involves high temperature to complete the transformation of the crystal structure of the film. In order to expedite the annealing time or deliver low-temperature processing for flexible devices using polymer substrates, excimer laser annealing is one of the preferred fast processing technologies. In the followed section, excimer laser annealing for TiO_2 crystallization would be described.

2.4.1 Excimer Laser Crystallization of TiO_2

Laser-Solid Interaction

Electromagnetic radiation with wavelength ranging from ultraviolet to infrared interacts exclusively with electrons, as atoms are too heavy to respond significantly to the high frequencies ($v > 10^{13}$ Hz) [70]. Therefore, the optical properties of material are determined by the energy states of its valence electrons. Bond electrons normally weakly respond to the external electromagnetic wave and affect only its phase velocity. However, free electrons can be accelerated and therefore extract energy from the field. Since the field is periodically changing, the oscillating electrons reradiate their kinetic energy or collide with the atoms, giving their energy to the lattice.

Absorption of incident energy fundamentally dictates the resultant thermal state of the material and therefore is a suitable point to begin an analysis of laser-solid interactions.

The mechanisms involved in absorption of incident radiation in materials are defined by the electronic structure of the material, and therefore it is useful to discuss exclusively semiconductors. In semiconductors, five distinct mechanisms for the absorption of light can be identified [71].

(1) Photons with energy (hv) much less than the band-gap energy (E_g) can excite lattice vibrations directly.

(2) Free or nearly free carriers can be excited by absorption of light with $hv < E_g$; such carriers will always be present as a result of finite temperature and doping.

(3) An induced metallic-like absorption due to free carriers generated by the laser radiation itself can occur.

(4) For photon energies are larger than E_g, absorption will take place by direct and indirect (photon-assisted) excitation of electron-hole pairs.

(5) Absorption induced by broken symmetry of the crystalline lattice is possible.

Here, the largest contributions to absorption of laser radiation with hv > Eg by crystalline or amorphous TiO_2 are found in mechanisms (4) and (5), respectively.

Eximer laser crystallization of TiO_2

The basic mechanism of laser heating proceeds is through photon absorption and the subsequent rapid transfer of energy from the electrons to the lattice. During laser annealing a beam of photons is focused on a sample. Simply put, the photons interact with the electrons in the sample which then transfer the energy to the lattice. This causes localized heating in the area where the photons hit the sample. More specifically, the

wavelength of this light determines how the energy will be absorbed in the TiO_2. The energy of the beam, or incident photon energy, is determined by the Eq. (2.5):

$$E = hc/\lambda \qquad (2.5)$$

where h is the Planck's constant (6.626×10^{-34} Js), c is the speed of light (3.00×10^8 m/s), and λ is the wavelength of the laser. Based on this equation, the photon energy from KrF excimer laser (λ=248 nm) is 5 eV. With the bandgap of TiO_2 around 3.0 eV, laser energy greater than this bandgap. When a beam of photons of energy hν > Eg is absorbed in a semiconductor, excited carriers, which results in lattice heating [72], is a complicated process and a field of active research [73]. Excited carrier relaxation times on the order of pico-seconds. As incident radiation is converted to increasing lattice temperatures, the thermophysical properties of the material dictate temperature distribution and phase changes. This aspect of laser annealing area has been actively investigated [74,75,76].
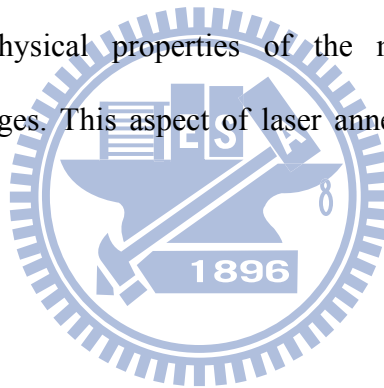
Table 2.1 Different TiO_2 polymorphs and some of their physical properties.

	Rutile	Anatase	Brookite
Crystal System	tetragonal	tetragonal	Orthorhombic
Density (g/cm$_3$)[37, 39]	4.13-4.26	3.79-3.84	3.99-4.11
Band-Gap (eV)[39]	3.0	3.2	3.11
Refractive Index [39]	2.72	2.52	2.63
Melting Point (^{o}C)	1855	Converts to rutile	Converts to rutile

Table 2.2 Average wall thickness and tube length of 10 V TiO$_2$ nanotube arrays anodized in HF aqueous electrolyte at different bath temperatures [58]

Anozization temperatures	Wall thickness (nm)	Tube length (nm)
5°C	34	224
25°C	24	176
35°C	13.5	156
50°C.	9	120
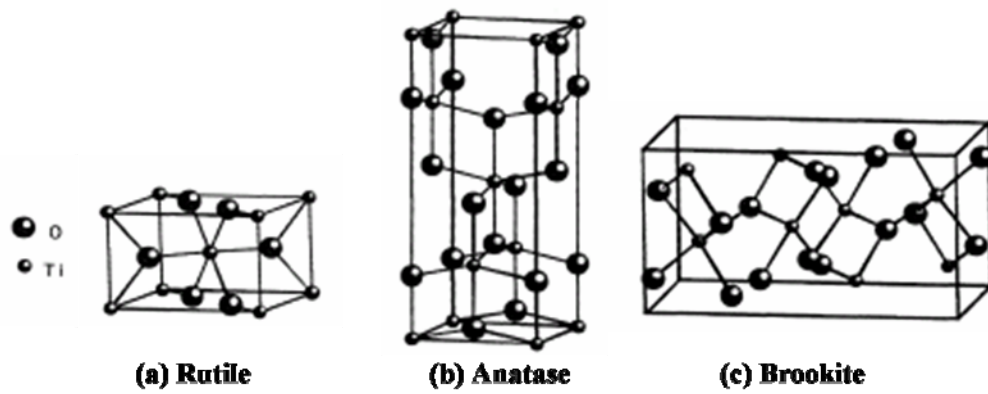
Figure 2.1 TiO$_2$ different crystal structures: (a) Rutile, (b)Anatase, and (c) Brookite [37].
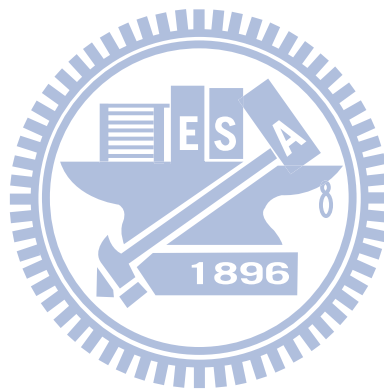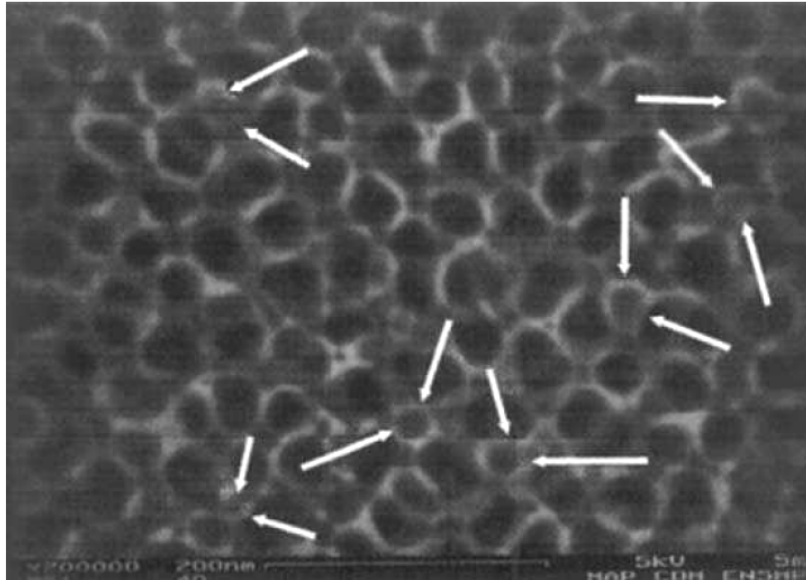
Figure 2.2 High resolution SEM image of anodized Ti_6Al_4V (TA6V) in CA/HF solution (10 V, 20 min) [28].
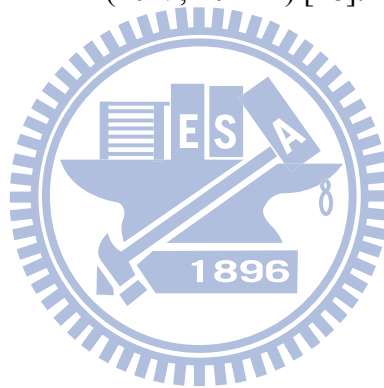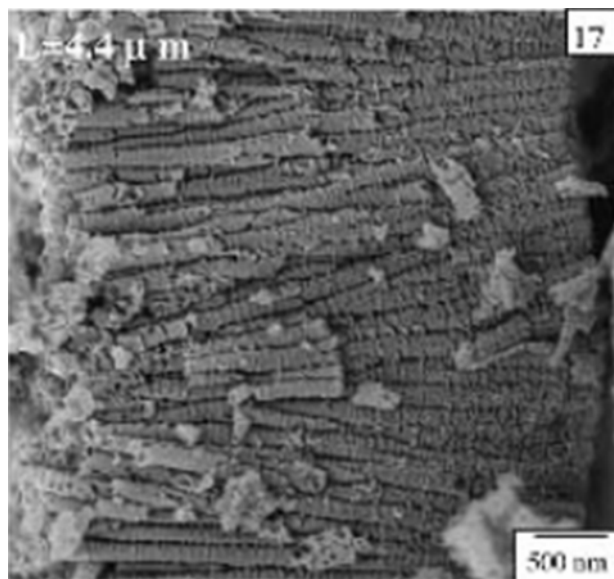
Figure 2.3 Lateral view of the nanotubes formed in 0.1M KF, 1M H_2SO_4, and 0.2M citric acid solutions(25V, 20h) [50].
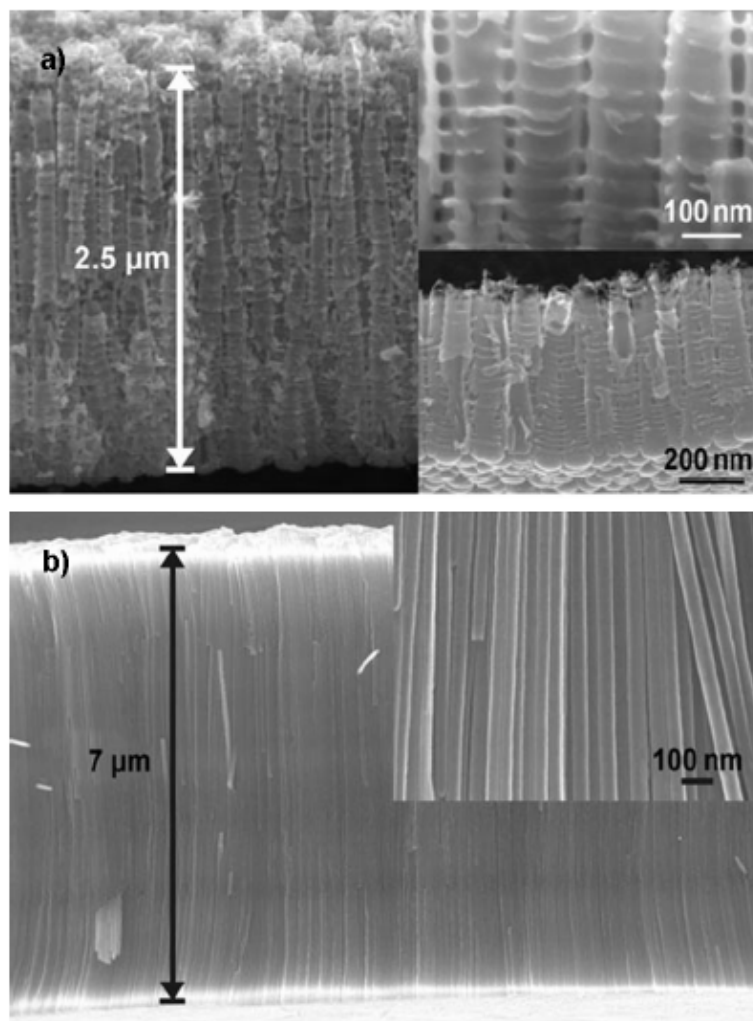
Figure 2.4 A comparison between SEM cross section images of nanotubes prepared in (a) an aqueous based and (b) organic electrolyte [30].
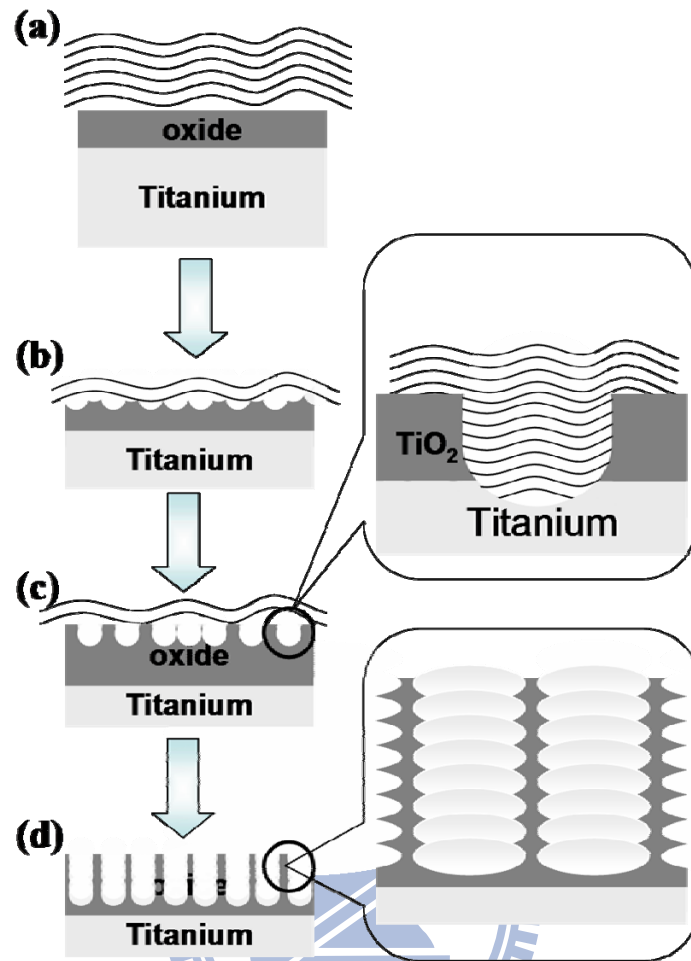
Figure 2.5 Schematic diagrams illustrating the formation mechanism of TiO_2 nanotubes structures (a) oxide layer formation, (b) semicircle pores formation on the oxide film, (c) growth of the semicircle pores into scallop shaped pores, and (d) fully developed nanotube arrays.
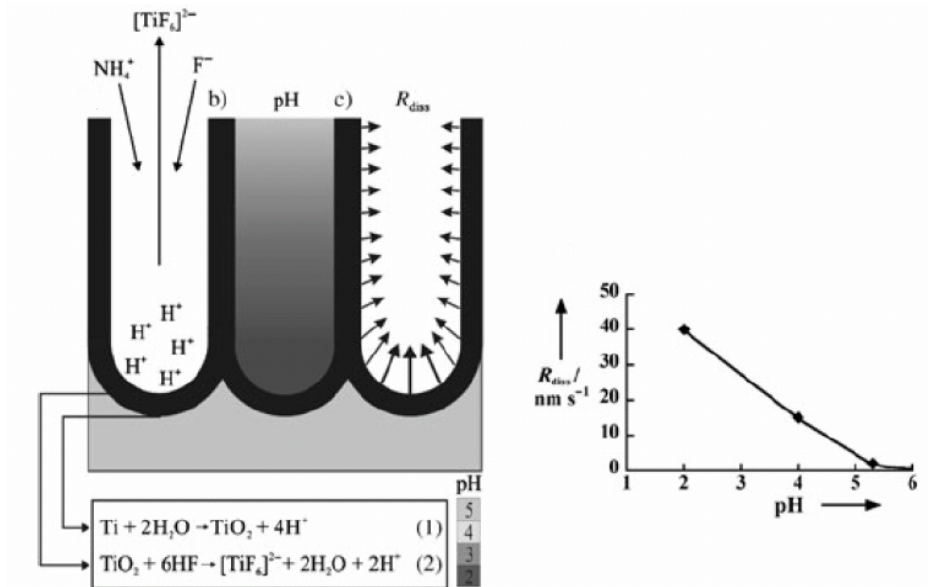
Figure 2.6 Schematic of the pH profile developing within the tubes [29].
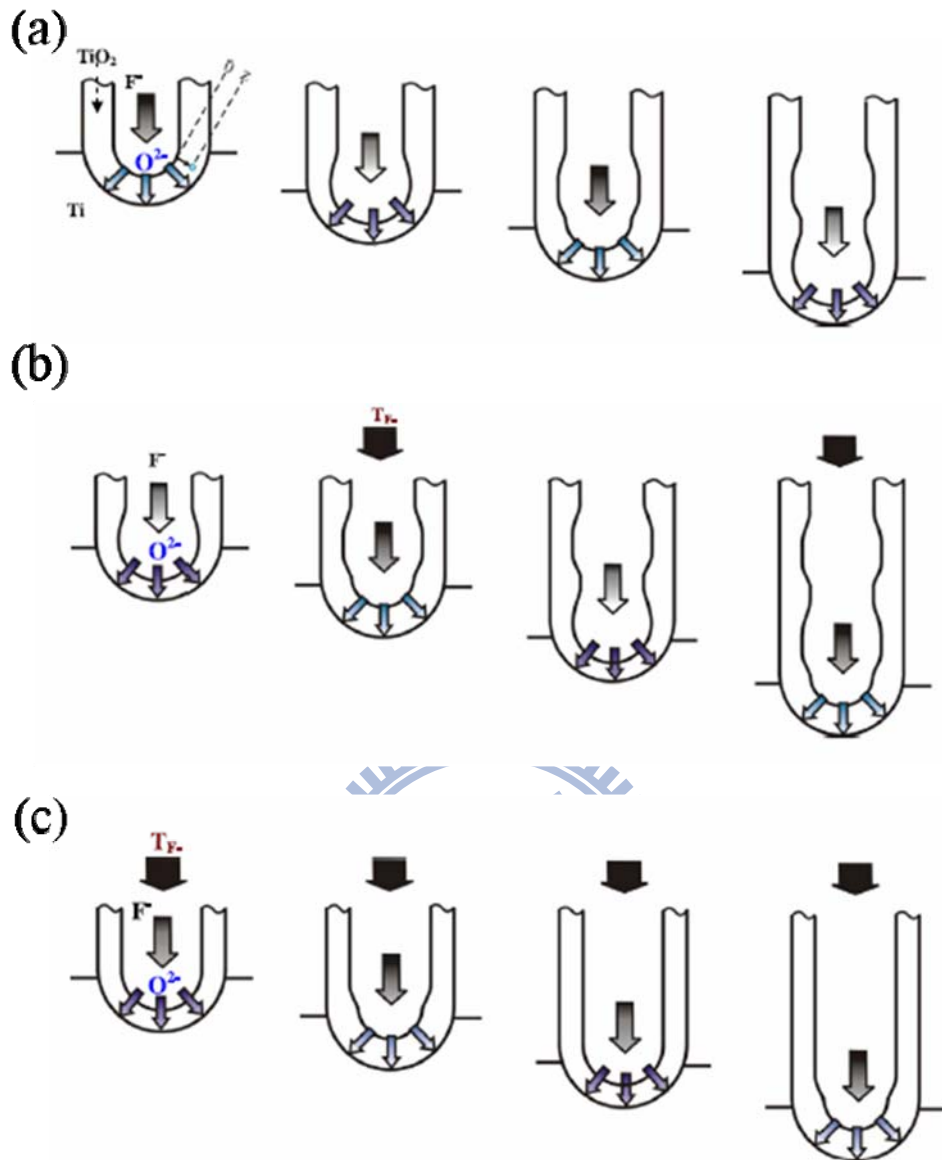
Figure 2.7 Schematic diagram of the formation of tube spatial periodicity under different conditions: (a) without stirring, (b) at medium stirring rate, and (c) at high stirring rate [57].
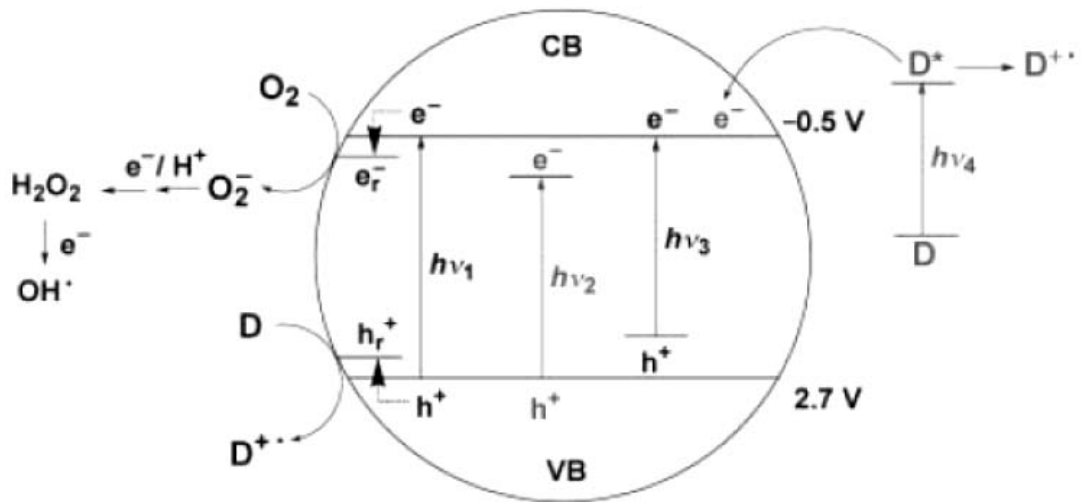
Figure 2.8 Mechanistic principles for the degradation of pollutants.

Chapter 3 Experimental Section

3.1 Materials candidates

3.1.1 TiO$_2$ nanotubes arrays structure (TNAs)

Titanium foil 99.9% purity, 0.5 mm thickness and sample size 1×1.5 cm^2 was used as the substrate for forming TiO$_2$ layer by anodic oxidation. Prior to anodization, Ti foil was ultrasonically cleaned by distilled water, rinsed by acetone, and then dried by a purging N$_2$ gas. The schematic diagram of anodization reaction system is illustrated in Fig. 3.1. All anodization experiments were carried out at room temperature using a two-electrode electrochemical cell consisting of a stainless steel foil (SS304) as the cathode and a Ti foil as the anode, at a constant dc potential. Two different electrolyte compositions and their anodization conditions are (1) 0.25 wt % hydrofluoric acid solution 50% aqueous solution; samples anodized at 20 V for 4 h and (2) 0.5 wt % NH$_4$F dissolved in the ethylene glycol (EG) solution with 1 wt % H$_2$O; samples anodized at 20 V for 0.5 h. The height of TNAs prepared by HF and NH$_4$F electrolytes in this study was fixed at 500 nm, unless stated otherwise.

3.1.2 TiO$_2$ hybrid structure (TNAs/TNWs)

The TiO$_2$ nanotube arrays and nanowires were fabricated by using electrolytes consisting of EG and water (99:1 in wt%) with 0.5 wt% NH$_4$F. The process conditions of anodizing voltage and processing time were selected to elucidate the formation mechanism of TNWs/TNAs structures. First, the anodizing voltage was varied from 20 to 80 V, while the processing time was maintained at 1 h. Then, an anodizing voltage of 40 V was used, while the anodization time was increased from 30 min to 120 min.

3.2 Post annealing of TiO₂

After fabrication, the samples were annealed by conventional furnace and excimer laser annealing; Following section will described the detail of two annealed technologies.

3.2.1 Conventional furnace annealing

In conventional furnace annealing, the TiO_2/Ti samples were annealed in ambient. A tungsten wire heater was rolled around the quartz tube to create a homogeneous temperature in the furnace. After TNAs fabrication, thermal annealing was performed in ambient air at 400 ^{o}C for 1 h under a heating rate of 2 ^{o}C/min.

3.2.2 Excimer laser annealing

The Laser annealing system was performed with a KrF excimer laser operated at a 248 nm wavelength (Lambda Physik Complex 201), 25 ns (FWHM) pulse width and 10 Hz repetition rate. The schematic diagram of KrF excimer laser system are illustrated in Fig. 3.2. The diameter of the laser beam was adjusted to 0.5×1.5 cm^2 to ensure full coverage onto the TNAs samples (sample size is 1×1.5 cm^2) by two separate exposures. The laser annealing conditions were selected to elucidate the structural and morphological transformation of TNAs by changing the laser fluence from 67, 125, 133, 267 to 400 mJ/cm^2 under the same number of 9000 shots. In this study, we also used two laser-sample irradiation modes for laser annealing of TNAs: (1) parallel mode and (2) tilted mode as schematically illustrated in Figs. 3.3(a) and 3.3(b), respectively. In the parallel mode (Fig. 3.3(a)), the angle α between the laser beam and sample was set at 90° with a fixed substrate holder. In the tilted mode (Fig. 3.3(b)), the angle α (0° - 90°) was varied from 30° to 85° in this study. In addition, the sample was rotated 40° manually around the axis of the laser beam for every 1000 shots to deliver a total of 9000 shots with

uniformity. In order to compare any difference in the structure and morphology between laser annealing and conventional annealing, conventional annealing of TNAs samples was carried out using a furnace in air atmosphere at 400°C for 1 hr.

3.3 Characterization of key propertirs

3.3.1 Morphology and microstructure characterization of the TNAs

The surface and cross-section morphology of TNAs were examined using a field emission scanning electron microscope (FESEM) (JOEL JSM-6700)), which was operated at an accelerating voltage of 15.0 kV, and a focused ion beam scanning electron microscope (FIB/SEM) (FEI Nova-200), which was operated at an accelerating voltage of 5.0 kV. An X-ray diffractometer (XRD) (Siemens Diffractometer D5000) with Cu Kα (λ=1.5405Å) radiation was employed to analyze the crystal structure of the TNAs films. In addition, transmission electron microscope (TEM) images and selected area diffraction (SAD) patterns of TNAs were obtained by a high-resolution transmission electron microscope (HRTEM) (JEOL 2010) at 200 kV.

3.3.2 X-ray absorption spectroscopy

The X-ray absorption near-edge structure spectroscopy (XANES) measurements were performed using the beam line 20A of National Synchrotron Radiation Research Center (NSRRC), Hsinchu, Taiwan. The XANES spectra were collected in the vicinity of titanium L-edge (450-490 eV) and oxygen K-edge (520-570 eV) regions. All spectra in this paper were measured in total electron yield mode using a high-energy spherical grating monochrometer with energy resolution ~70 meV or better for 6m-HSGM beamline at 400 eV [77]. All spectra were collected at room temperature, while the chamber pressure was kept at about 2×10^{-8} Torr or better. The incoming radiation flux was monitored by the total photocurrent produced in a clean Au mesh inserted into the

beam. The energy scale in the XAS spectra was calibrated by using the known peak positions of a $SrTiO_3$. The resolution of the Ti $L_{2,3}$ and O K-edge XAS spectra was ~100 meV. In order to compare different oxidation states of titanium, we have also measured the Ti L-edge and O K-edge of TiO (99.9%, Strem Chemical) and Ti_2O_3 (99.8%, Alfa Aesar). Quantitative analysis of crystalline, amorphous phases, and suboxides in TNAs were obtained from the intensity ratios of relevant orbitals in the O K-edge based on the published spectra [78,79,80,81]. Specifically, a commercial curve-fitting software (PeakFit v4.12, SeaSolve, USA) was used to determine the intensities of TiO, Ti_2O_3, TiO_2 (anatase), and TiO_2 (amorphous) patterns by using a Gaussian-Lorentzian function. The error of the fitting was minimized by repeating the curve fitting procedure to yield a coefficient of determination (R^2) greater than 0.96.

3.3.3 Surface areas measurement

The surface areas of the TNWs/TNAs films were measured by dye (N719 dye, Solaronix) adsorption, which is a commonly used method in DSSC applications [82].Specifically, the amount of dye adsorption was determined by desorbing the dye from the TiO_2 films into 5 mM NaOH aqueous solution. The quantification was based on the dye's maximum absorption values at 515 nm in the dye-desorbed NaOH solutions as measured by an UV-visible light spectrometer (Evolution 300), using a dye solution of concentration 8×10^{-2} mM as a reference.

3.4 Photocatalytic reaction experiments

For the photocatalytic reaction experiments, the TNWs/TNAs film on Ti substrate of 2×1 cm^2 size was immersed in a quartz cuvette containing 10 ml methylene blue (MB) ($C_{16}H_{18}ClN_3S$, Acros Organics) solution with an initial concentration of 2.5×10^{-5} M. The samples were then irradiated by UV light at 360 nm using an 8W HeCd lamp (Sankyo

Denki Co., Japan). The decomposition rate of the MB in the solution along with TNWs/TNAs films, can be obtained by monitoring its absorbance periodically (every 4 h) using an UV/Vis spectrometer at wavelength 650 nm. The total height of the TNWs/TNAs was maintained at 12 ± 0.5 μm, in which the TNAs tube length was ~11 μm and the TNWs was ~1 μm in cross-section with a wire length of ~5-10 μm.
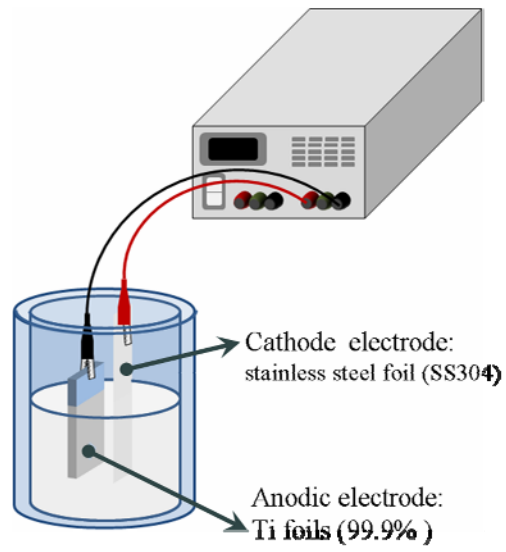
Figure 3.1 Schematic diagram of anodization reaction system
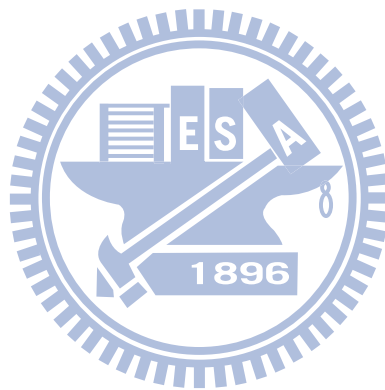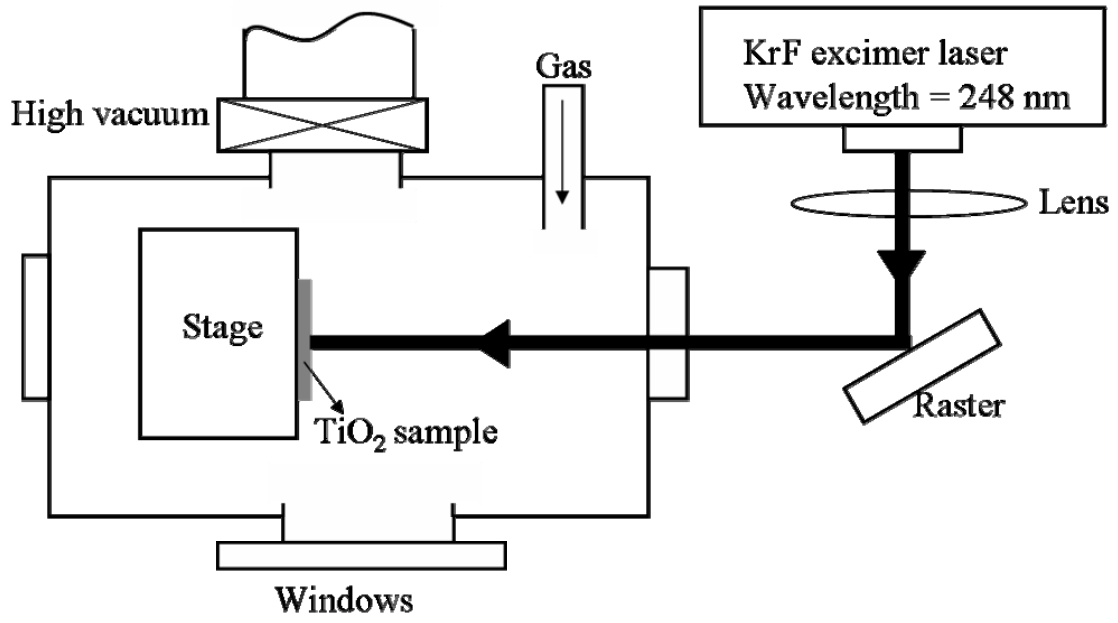
Figure 3.2 The schematic diagram of KrF excimer laser system
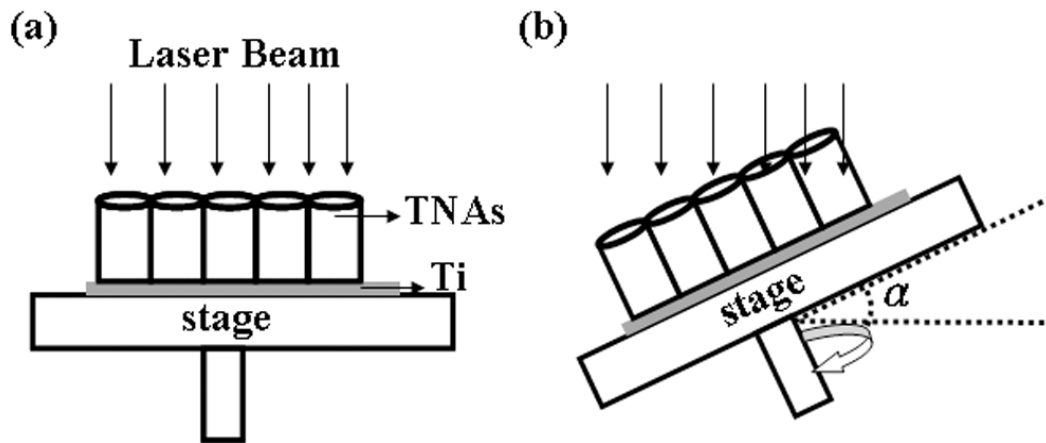
Figure 3.3 Schematic diagrams of laser anneal systems for TNAs in (a) parallel mode and (b) tilted mode

Chapter 4

The evolution of microstructure and composition of TiO_2 nanotube arrays during annealing

4.1 Morphological observation

We first examined the surface and cross-section morphology of TNAs prepared by anodic oxidation in (a) HF solution and (b) NH_4F solution using SEM. As shown in Fig. 4.1(a) for HF solution system, the self-organized regular porous TiO_2 structure consists of pore arrays with a uniform pore diameter of approximately 70 nm and a wall thickness of 20 nm. TNAs of 500 nm (7:1 aspect ratio) in length were obtained in a 0.25 wt% HF solution at room temperature and 20V working voltage for 4 h. However, the length (~500 nm) of nanotubes did not increase with anodization time in HF solution because the high hydroxyl concentrations increased the electrochemical etching rate [28].

In order to obtain TiO_2 nanotubes with high aspect ratio, we used a high-viscosity ethylene glycol electrolyte with 0.5 wt% NH_4F and 1 wt% H_2O. Surface morphology of TiO_2 nanotube structure with treatment time of 24 hours shows smaller tube diameter of 40 nm, same wall thickness (~20 nm), and tube length of 7 μm (170:1 high aspect ratio), as illustrated in Fig. 4.1(b). This clearly shows that the electrolyte is the crucial factor controlling the nanotube morphology and its growth rate. The key for achieving high-aspect-ratio growth was to adjust the ionic diffusion coefficient of electrolyte, which was responsible for maintaining a high H^+ concentration at the pore bottom with a protective environment maintained along the pore walls and at the pore mouth during chemical drilling [29]. For the rest of this study, TNAs with 500 nm height were used

for comparison. Surface morphology of TNAs prepared by NH$_4$F electrolyte illustrated in Fig. 4.1(c) shows tube diameter of 40 nm, wall thickness of 20 nm, and tube length of 500 nm after treatment time of only 0.5h.

4.2 Microstructure and composition of TNAs

4.2.1 XRD analysis

Following morphological observation, the microstructure of TNAs was examined by XRD analysis. Figure 4.2 shows that TNAs prepared in (a) HF solution and (b) NH$_4$F solution as-grown and annealing to 100°C are both in fully amorphous phase. In the HF system, the anatase phase was formed when annealing temperature was $\geq$ 200°C, and the intensity of anatase (101) peak increased with increasing temperature up to 400°C. In contrast, in the NH$_4$F system, when TNAs was annealed up to 200°C, the spectrum remained the same as that of as-grown, showing no change in amorphous TiO$_2$. There was no evidence for the presence of either rutile or anatase phase for annealing temperature at 200°C. This was noticeably different from TNAs as-grown in HF solution, which was converted into crystalline TiO$_2$ after annealing at 200°C. However, when the annealing temperature was raised to 300°C, the anatase phase appeared and the intensity of anatase (101) peak increased with increasing temperature from 300 to 400°C. This illustrated that a sufficient annealing energy, *i.e.* annealing temperature, must be imparted to transform as-grown amorphous TiO$_2$ into anatase phase, and that the amount of anatase phase in TiO$_2$ nanotube films increased with increasing annealing temperature. However, XRD cannot distinguish any suboxides in the amorphous TiO$_2$ structure as-grown by HF or NH$_4$F system at room temperature and after subsequent annealing. Therefore, XANES will be employed to quantitatively

analyze the electronic states in different polymorphs and oxidation states of TiO_2 array nanotube in the following section.

4.2.2 XANES analysis

4.2.2.1 Ti $L_{2,3}$ edge XANES spectra

Figure 4.3 illustrates Ti $L_{2,3}$-edge XANES spectra of TNAs as-grown in HF solution and post annealed to various temperatures ranging from 100 to 400 ^oC. There were four dominant features, which could be attributed to excitations of Ti $2p_{3/2}$ (L_3-edge) and Ti $2p_{1/2}$ (L_2-edge) core levels into empty Ti 3d states. For TNAs as-grown in HF solution at room temperature, the $L_{2,3}$-edge showed broad features with low intensities in t_{2g} and structureless e_g, which were indicative of amorphous TiO_2 [83]. The peak broadening was attributed to a loss of the long-range order due to the effects of interactions of titanium with second-neighbor atoms [35]. When as-grown TiO_2 was annealed to 100, 200, 300, and 400 ^oC, the spectra instead showed definite crystalline structures as indicated by the sharpness and higher t_{2g} orbitals and double features of e_g orbitals in L_3 edge. In addition, the leading edge of the Ti L-edge shifted 0.3 eV to higher energy. The increase in Ti $2p_{3/2}$ binding energy implied that Ti had changed from lower charge states Ti^0, Ti^{+2} or Ti^{+3} to Ti^{4+} (TiO_2) [84]. This suggests that TNAs prepared at room temperature contain not only amorphous TiO_2 but also some lower oxidation states of titanium such as TiO and Ti_2O_3, which undergo oxidation during annealing, thus causing the Ti L-edge shift to higher energy.

Table 4.1 summarizes the intensity ratios of orbitals for Ti L_3 edge of TNAs prepared by anodic oxidation as-grown in HF and NH_4F solutions and subsequently annealed to 100, 200, 300, and 400^oC. As illustrated in Fig. 4.3 and Table 4.1, for all TiO_2 polymorphs, the intensity ratio of $I(L_3\text{-}t_{2g})/I(L_3\text{-}e_g)$ increases from 0.78 to

0.98-1.01 as the annealing temperature is raised to 200, 300, and 400°C. Since the intensity of the L-edge features varied with the density of empty d-states, an increase of I(L$_3$-t$_{2g}$)/I(L$_3$-e$_g$) intensity ratio implied an empty state in t$_{2g}$ orbitals, which was consistent with an increase in Ti^{4+} cations [85]. Thus, annealing in oxygen atmosphere led to enhance oxidation of Ti cations to form TiO$_2$. On the other hand, the e$_g$-related peak of the L$_3$ edge was split into two peaks (b$_1$ and b$_2$) at 461 eV as the annealing temperature is increased to 200°C. This showed that the major differences between Ti L$_{2,3}$-edge spectra of amorphous and crystalline phases of TiO$_2$ were significant changes in positions, intensities, and widths of e$_g$-related peaks b$_1$ and b$_2$. For instance, in anatase, the intensity of peak b$_1$ is substantially stronger than that of peak b$_2$; while in rutile, the intensity of peak b$_2$ is substantially stronger than that of peak b$_1$ [84]. When the annealing temperature was further raised from 200 to 400°C, the I(b$_1$)/I(b$_2$) intensity ratio was increased from 1.01 to 1.10. Based on I(t$_{2g}$)/I(e$_g$) and I (b$_1$)/I(b$_2$) intensity ratios in the published literature [85], we can conclude that with increasing annealing temperature, more TNAs were transformed towards anatase TiO$_2$.

The Ti L$_{2,3}$ edge XANES spectra of TNAs as-grown in NH$_4$F solution and annealed to various temperatures ranging from 100 to 400°C are shown in Fig. 4.4. As-grown nanotube arrays at room temperature showed no obvious difference from the TNAs prepared in HF solution. Both Ti L$_{2,3}$ edge spectra showed the characteristics of amorphous TiO$_2$ with broad structures, low intensity of t$_{2g}$, and structureless e$_g$. When TNAs were annealed at 200°C, the spectrum remained the same as that of as-grown at room temperature, showing no change in amorphous TiO$_2$ characteristics upon anneal under oxygen environment. This was in striking contrast to TNAs as-grown in HF solution, which had been converted into crystalline TiO$_2$ after annealing at 200°C. However, as the annealing temperature was raised to 300°C and above, sharpness and

41

higher t_{2g} orbitals and double features of e_g orbitals (labeled as b_1 and b_2) appeared, in addition to Ti L-edge shifting to higher energy. The results suggested that TNAs grown at room temperature or even annealing at 200°C, possessed primarily amorphous TiO_2 and some suboxides such as TiO and Ti_2O_3. As the annealing temperature was increased to 300°C and above, the spectrum showed that the structure has transformed from amorphous to anatase TiO_2 as indicated by the sharpness and higher t_{2g} orbitals and e_g orbitals of the L_3-edge.

Figure 4.4 and Table 4.1 show that annealing treatment changes the intensity ratio of L_3-t_{2g}/L_3-e_g from 0.79 at room temperature to 0.86 at 200 °C, to 0.99-1.02 at 300 and 400°C, respectively. It indicated that annealing in oxygen atmosphere led to more Ti L_3-t_{2g} features, which were TiO_2 formed by enhanced oxidation with Ti cations. Moreover, the e_g-related peak of the L_3 edge was further split into two peaks only after annealing temperature was raised to 300°C and above. The $I(b_1)/I(b_2)$ intensity ratio was increased to 1.11 and 1.10 for annealing temperature of 300 and 400 °C, respectively. As a result, it is clear that the onset temperature of phase transformation of TNAs prepared in NH_4F solution was higher than those prepared by HF solution. Moreover, taking $I(t_{2g})/I(e_g)$ and $I(b_1)/I(b_2)$ intensity ratios into account, we found that the crystallinity percentage in TNAs increased with increasing annealing temperature, presumably due to phase transformation and the oxidation of existing defects such as TiO and Ti_2O_3. Their quantities as a function of annealing temperature and electrolytes warrants our attention for further XANES analysis based on oxygen 1s (K-edge) absorption in the subsequent section.

4.2.2.2 Oxygen 1s (K-edge) absorption

Oxygen 1s (K-edge) absorption involving the excitation of an oxygen 1s electron into unoccupied 2p-states, was employed to map out the oxygen 2p-projected density of unoccupied states in order to examine the oxidation states and crystalline phases of TNAs. Figure 4.5 compares the O K-edge XANES spectra of TNAs prepared by anodic oxidation as-grown in (a) HF and (b) NH_4F solution and post annealed to 100, 200, 300, and 400 ^{o}C. There were two dominant features in lower energy, 530-536 eV in the O K-edge spectra, which could be assigned to the transitions into Ti 3d t_{2g} and e_g levels [86,87]. Broad peaks were observed for TNAs in HF and NH_4F system lower than 100 ^{o}C, and even for the sample prepared in NH_4F solution with post annealing at 200 ^{o}C. Such an inhomogeneous broadening caused by slight variations in bond lengths and angles, is inherent to spectra of amorphous TiO_2 solids [79]. However, after annealing to 200 ^{o}C for HF system and 300 ^{o}C for NH_4F system, higher temperature led to more distinct and narrow shapes of Ti 3d t_{2g} and e_g features. Also, a new peak appeared at higher energy (539.3 eV), which could be attributed to transitions into 4sp orbitals, indicative of anatase-phase TiO_2 [88].

It is worthwhile to note that the energy separation of both t_{2g} and e_g orbitals provides a direct measure of the ligand-field splitting (LFS) of TiO_2. The LFS for various oxidation states of oxygen K-edge spectra, revealed a deceasing trend in the sequence of TiO_2 (2.6-2.7 eV), Ti_2O_3 (2.2 eV), and TiO (1.5 eV) [85,89]. For TNAs prepared in HF system shown in Fig. 4.5(a), LFS increased from 2.5 eV for as-grown to 2.6 eV for annealing temperature $\geq$ 200°C. When the electrolyte was changed to NH_4F solution, the spectrum of as-grown revealed a LFS of 2.3 eV as illustrated in Fig. 4.5(b). Upon annealing, LSF sill remained at 2.3 eV at 200°C, then increased to 2.6 eV as

annealing temperature was raised to 300°C and above. The lower LSF for annealing temperature at ≤ 200°C showed the existence of lower oxidation states such as Ti_2O_3 and TiO. Upon further annealing, there was a continued charge transfer from Ti^{+2} or Ti^{+3} cations to Ti^{4+}.

Figure 4.6 compares the O K-edge XANES spectra of TNAs as-grown in HF solution and after annealing to 100, 200, 300, and 400°C. As shown in Fig. 4.6(a), there are 90% for TiO_2 amorphous phase and about 10% suboxides for Ti^{2+} (TiO) and Ti^{3+} (Ti_2O_3) cations in as-grown at room temperature. As the annealing temperature was increased to 200°C as shown in Fig. 4.6(b), amorphous phase (90% as-grown) was mostly transformed to anatase phase (85%), in addition to a reduction of suboxides from 10% to 3% through charge transfer of Ti^{+2} or Ti^{+3} cations to Ti^{+4} cations. As annealing temperature was increased to 300 or 400°C illustrated in Figs. 4.6(c) and 6(d), the continued charge transfer of Ti from lower charge state, Ti^{+2} or Ti^{+3} to Ti^{4+} further reduced the amount of suboxides to 1%, while the percentage of crystallinity of TNAs was increased to 93% for anatase phase.

Figure 4.7 shows the O K-edge XANES spectra of TNAs in NH_4F solution for as-grown and annealing at 100, 200, 300, and 400°C. As illustrated in Fig. 4.7(a), the fitting spectra shows that as-grown TNAs at room temperature possesses 82% TiO_2 amorphous phase and 18% suboxides for Ti^{2+} (TiO) and Ti^{3+} (Ti_2O_3) cations. The lower percentage of amorphous TiO_2 in NH_4F system in as-grown nanotube arrays compared to that in HF system can be attributed to lower oxygen ion formation from a scanty 1 wt% H_2O addition in the solution. As the annealing temperature is increased to 200°C as shown in Fig. 4.7(b), there is still a large amount of TiO_2 amorphous phase (89%) and 11% suboxides (4% TiO and 7% Ti_2O_3 cations). Further increase to 300°C as shown in

Fig. 4.7(c), the phase transformation has taken place from amorphous to anatase phase (80%), in addition to a reduction of suboxides from 11% to 7%. As annealing temperature was increased to 400°C, the percentage of crystallinity for anatase roses to 86%, while the amount of suboxides reduced further to 4% (Ti_2O_3). From these results, we can conclude that with increasing annealing temperature to 400°C, the percentage of crystallinity of TNAs was increased only up to 86% for the anatase phase. Moreover, the onset temperature for the phase transformation of TNAs prepared in NH_4F solution was higher than those prepared by HF solution.

Table 4.2 summarizes the amount of crystalline, amorphous phases and composition of TNAs as grown and after annealing to 200, 300, and 400 °C. First, in HF solution, there were 90% for TiO_2 amorphous phase, 2% TiO, and 8% Ti_2O_3 in as-grown TNAs at room temperature. As the annealing temperature was increased to 200°C, this additional energy enabled phase transformation from amorphous phase to anatase phase (85%), and also reduced the suboxides from 10% to 3% (1% TiO and 2% Ti_2O_3) by charge transfer to Ti^{4+} cations. When temperature was further increased to 300 or 400°C, Ti has changed from the lower charge state Ti^{+2} or Ti^{+3} to Ti^{4+}, reducing the amount of suboxides to 1% (0% TiO and 1% Ti_2O_3) but increasing the crystallinity of TNAs to 93% anatase phase. However, in NH_4F system, because lower oxygen ion formation from the scanty 1 wt% H_2O addition, there were 18% suboxides (7% TiO and 11% Ti_2O_3) in as-grown TNAs at room temperature. Even after annealing to 200°C, there was only charge transfer of Ti cations from lower charge state Ti^{+2} or Ti^{+3} to Ti^{4+}, leading to 89% amorphous TiO_2 and still 11% suboxides consisting of 7% TiO and 4% Ti_2O_3. Further increase of energy to 300 and 400°C, the phase transformation had happened from amorphous phase to anatase phase (80% at 300°C and 86% at 400°C), in addition to a reduction of suboxides from 7% (3% TiO and 4% Ti_2O_3) to 4% (4%

45

Ti$_2$O$_3$). From the results, we find that the crystallinity of TiO$_2$ anatase phase was limited to 86% as annealing was raised to 400°C. The reason for the reduced crystallinity of TiO$_2$ anatase phase is due to the use of NH$_4$F. It is proposed that NH$_4$F dissociates to form NH$_4^+$ and F$^-$ first. Then F$^-$ reacts with H$^+$ to form HF, while NH$_4^+$ ions would form another suboxides. NH$_4^+$ would react with TiF$_6^{2-}$ to form (NH$_4$)$_2$TiF$_6$ type compounds [90]. Upon annealing, (NH$_4$)$_2$TiF$_6$ would decompose into NH$_4$TiOF$_3$ and TiOF$_2$ at first [91]. Further increase in the annealing temperature under oxygen environment, NH$_4$TiOF$_3$ and TiOF$_2$ are oxidized to form amorphous TiO$_2$, which in turn undergoes phase transformation to anatase TiO$_2$. Hence, the formation of (NH$_4$)$_2$TiF$_6$ compound is the important factor limiting the percentage of anatase crystallinity of TNAs prepared by NH$_4$F solution.

4.3 Summary

The electronic structures of TNAs have been examined by soft x-ray absorption near-edge structure spectroscopy around Ti $L_{2,3}$-edge and O K edge, in addition to XRD and SEM analyses on crystallinity and morphology. The main conclusions of this study can be summarized as follows.

TNAs as-grown in HF electrolyte were shown to contain 90% amorphous TiO_2 and 10% lower oxidation states of titanium from Ti^{2+} (TiO) and Ti^{3+} (Ti_2O_3) cations. After heat treatment at 400°C, TNAs underwent charge transfer and phase transformation to 93% anatase phase, 6% amorphous TiO_2, and 1% suboxides. In contrast, as-grown TNAs in NH_4F solution were found to possess 82% amorphous TiO_2 and higher suboxides (18%) due to lower oxygen ion formation from scanty 3% H_2O addition. The onset temperature of phase transformation of TNAs prepared in NH_4F solution was also found to be higher than those prepared by HF solution. Moreover, when annealed to 400°C, the crystallinity of TNAs increased only to 86% for the anatase phase. The lower anatase phase could be attributed to the formation of $(NH_4)_2TiF_6$ type compounds presumably formed by the reaction of TiF_6^{2-} and NH_4^+ ions dissociated from NH_4F. With the increase of annealing temperature under oxygen environment, $(NH_4)_2TiF_6$ would decompose into $TiOF_2$ and NH_4TiOF_3, which are further oxidized to amorphous TiO_2 and in turn phase transformed to anatase TiO_2 in various degree.

Table 4.1 Intensity ratios of orbitals for Ti L_3 edge of TNAs prepared in HF and NH_4F electrolytes: as-grown and post annealing at various temperatures, compared to those of Ti, anatase and rutile TiO_2 from literatures.

Intensity ratio / Sample	HF system		NH_4F system	
	$I(t_{2g})/I(e_g)$	$I(b_1)/I(b_2)$	$I(t_{2g})/I(e_g)$	$I(b_1)/I(b_2)$
Ti	0.54	-	0.54	-
TNAs as-grown	0.78	-	0.79	-
TNAs annealed at 200 ^{o}C	1.01	1.01	0.86	-
TNAs annealed at 300 ^{o}C	0.99	1.08	1.02	1.11
TNAs annealed at 400 ^{o}C	0.98	1.10	0.99	1.10
TiO_2 (anatase) [85]	0.93	1.21	0.93	1.21
TiO_2 (rutile) [85]	1.20	0.89	1.20	0.89

Table 4.2 Fitting results for the amount of amorphous and crystalline phases, and composition of TNAs in HF and NH$_4$F solution as-grown and post annealed at various temperatures

Electrolyte	Anneal Temperature	Polymorphs of TiO$_2$ and composition, %			
		TiO	Ti$_2$O$_3$	Amorphous TiO$_2$	Anatase TiO$_2$
HF	As-grown 25°C	2	8	90	0
	200 ^{o}C	1	2	12	85
	300°C	1	1	12	86
	400°C	0	1	6	93
NH$_4$F	As-grown 25 ^{o}C	7	11	82	0
	200 ^{o}C	4	7	89	0
	300 ^{o}C	3	4	13	80
	400 ^{o}C	0	4	10	86

Figure 4.1 Cross-section and surface morphology of TiO$_2$ nanotube arrays prepared by anodic oxidation in (a) HF solution for 4 hr (b) NH$_4$F solution for 24h and (c) NH$_4$F solution for 0.5h.
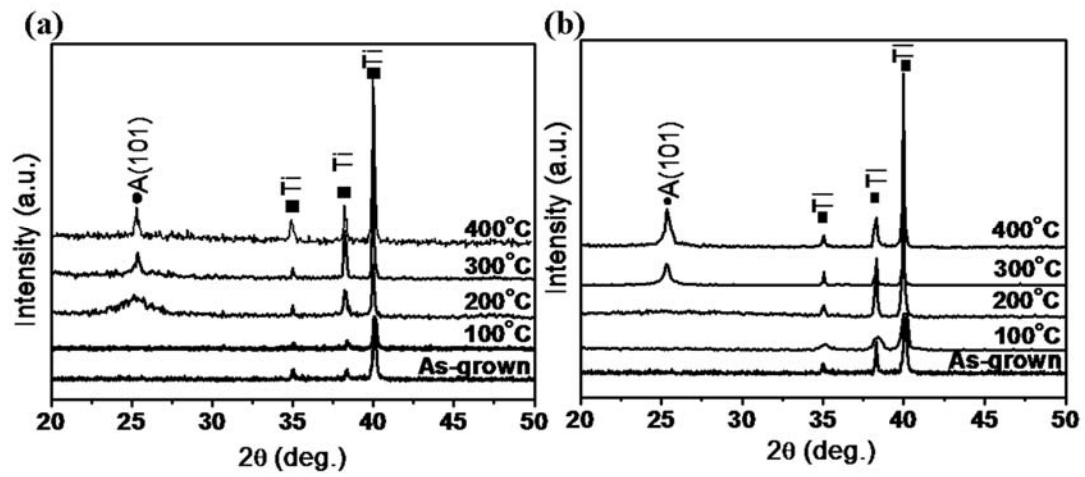
Figure 4.2 XRD patterns of the TiO$_2$ nanotube arrays prepared by anodic oxidation in (a) HF solution and (b) NH$_4$F solution: as-grown and post-annealing at 100, 200, 300, and 400 ^{o}C.
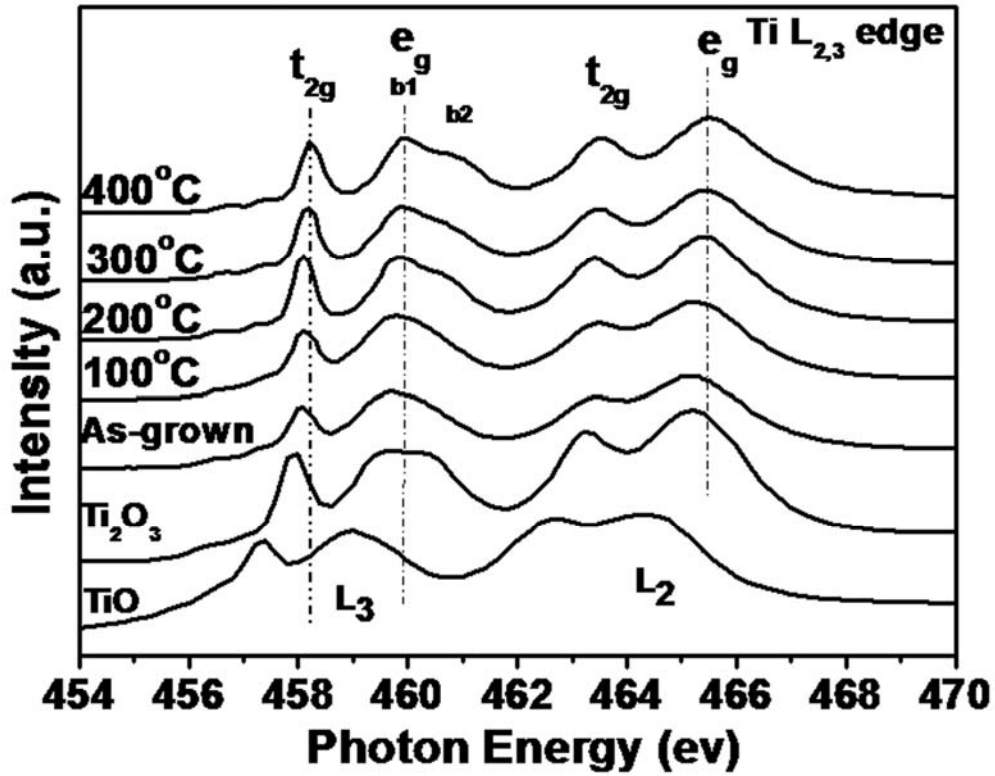
Figure 4.3 Ti $L_{2,3}$ edge XANES spectra of TiO, Ti_2O_3, and TiO_2 nanotube arrays prepared by anodic oxidation in HF solution: as-grown and post-annealing at 100, 200, 300, and 400 ^{o}C.
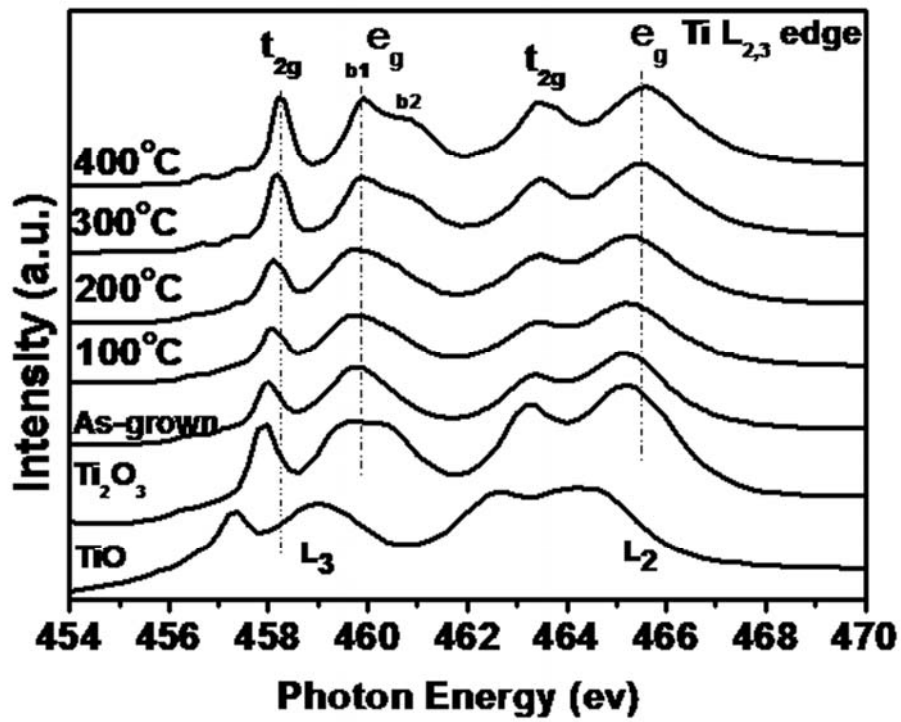
Figure 4.4 Ti L2,3 edge XANES spectra of TiO, Ti_2O_3, and TiO_2 nanotube arrays prepared by anodic oxidation in NH_4F solution: as-grown and post annealing at 100, 200, 300, and 400 ^oC.
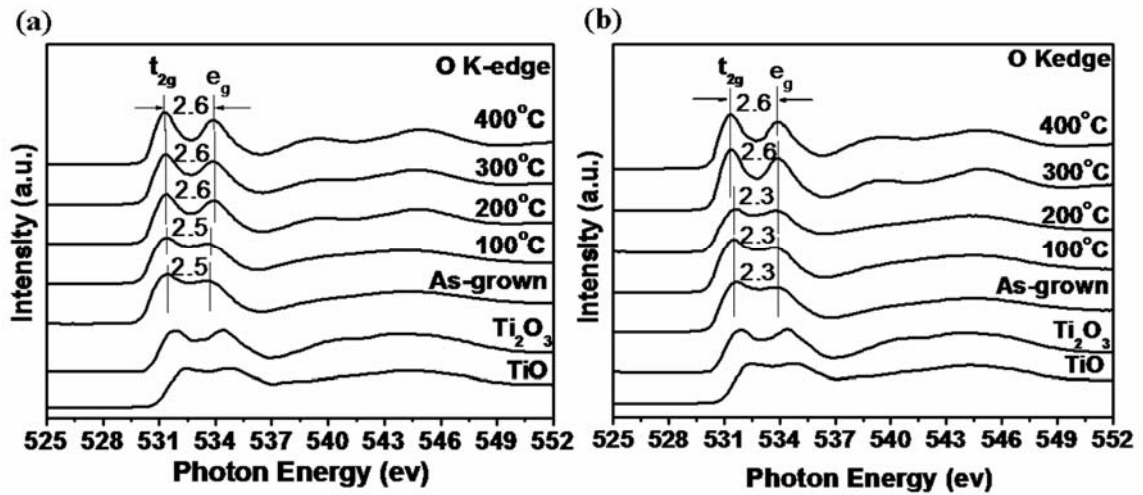
Figure 4.5 O K edge XANES spectra of TiO, Ti$_2$O$_3$, and TiO$_2$ nanotube arrays prepared by anodic oxidation in (a) HF solution and (b) NH$_4$F solution: as-grown and post-annealing at 100, 200, 300, and 400 ^{o}C.
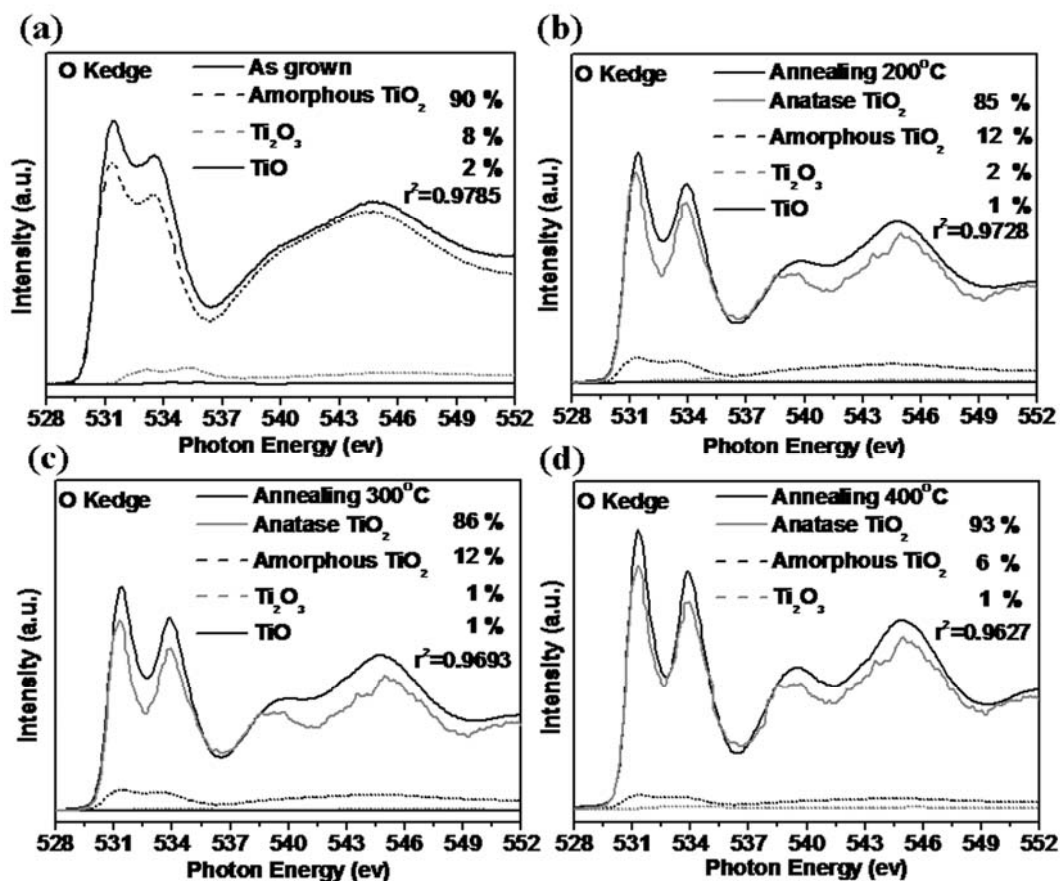
Figure 4.6 Fitting results for the O K-edge XANES spectra of TiO$_2$ nanotube arrays prepared by anodic oxidation in HF solution: (a) as-grown, and post-annealing at (b) 200 ^{o}C, (c) 300 ^{o}C, and (d) 400 ^{o}C.

Figure 4.7 Fitting results for the O K-edge XANES spectra of TiO$_2$ nano-tube arrays prepared by anodic oxidation in NH$_4$F solution: (a) as-grown, and post-annealing at (b) 200 °C, (c) 300 °C, and (d) 400 °C.

Chapter 5

Structural and morphological transformation of TiO$_2$ nanotube arrays induced by excimer laser treatment

5.1 ELA treatment of TNAs in a parallel mode

51.1 XRD microstructure analysis

We first examined the laser fluence effect on TNAs prepared by anodic oxidation in parallel mode. Figure 5.1 shows the XRD patterns of TNAs prepared by anodic oxidation as-grown in NH$_4$F solution and post annealing by excimer laser with various fluences at a total of 9000 shots. Results showed that the as-grown TNAs were fully amorphous because only the diffraction peaks from Ti substrate were detected. After irradiation of the TNAs with the excimer laser at 67 mJ/cm² laser fluence, the anatase phase appeared and the intensity of anatase (101) peak increased with increasing laser fluence up to 125 mJ/cm^2. As the fluence was further increased to $\geq$ 133 mJ/cm^2, the TNAs film exhibited not only anatase (101) and (200) peaks, but also rutile (110), (101), and (111) peaks. The mechanism of the ELA TiO$_2$ crystallization process has been reported by Van Overschelde et al. [92]. The absorption of light occurs by exciting of the electrons from occupied to unoccupied energy states. This is because the photon energy, hν, is larger than the fundamental bandgaps of various TiO$_2$ phases (E$_g$ are 3.0 eV for rutile, and 3.2 for anatase) [93]. The absorption of light creates an electron-hole pair by exciting an electron from the valence band into the conduction band. Since the optically excited states were obviously unstable, the system decays through a combination of various processes involving electrons, phonons, and atoms (or vacancies) which contribute to the heating of the lattices of the TiO$_2$ sample. When the heating is sufficient to overcome the

nucleation barrier, phase transitions may occur. Hence, in this case, the laser energy overcame the nucleation barrier for transformation of amorphous TiO_2 to anatase and possibly rutile phase. In addition, the amount of crystallinity of TNAs films increased with increasing laser fluence.

5.1.2 Morphological observation

The surface and cross-section morphology evolution of the TNAs annealed by excimer laser with various fluences were examined by SEM as shown in Fig. 5.2. A gradual change in surface morphology with increasing laser fluence was observed. For laser annealing under the laser fluence at 67 mJ/cm^2 (Fig. 5.2(a)), the surface morphology of highly ordered nanotube structure showed only slight damage, while the bulk of the nanotube arrays still remained intact. As the fluence was increased to 125 and 133 mJ/cm^2 (Fig. 5.2(b) and 5.2(c)), significant roughening and flower-like layers were observed on the top surface. As the fluence was further increased to 267 mJ/cm^2 (Fig. 5.2(d)), a re-solidified layer was formed on the surface, which sealed off some of the opening of the nanotubes. Finally, such morphology became more obvious for the samples treated at 400 mJ/cm^2 (Fig. 5.2(e)), while the bulk of the nanotube arrays remained intact. In short, the surface temperature of TiO_2 increased with increasing laser fluence [94], and the melting temperature of TiO_2 was reached as the laser fluence surpassed 125 mJ/cm^2. When the laser fluence was increased to $\geq$125 mJ/cm^2, the laser induced melting and coalescence near the surface, resulting in a flower-like, re-solidified layer. With increasing fluence, the re-solidified zone became larger.

On the other hand, the cross-sectional SEM images in Figs. 5.2(a) to 5.2(e) show that the thicknesses of the TNAs do not obviously change as a function of fluence. As a result, the laser damage is limited to the area near the surface with a flower-like, re-solidified

layer when higher laser fluence ($\geq$125 mJ/cm^2) is used. This damage near the surface could be attributed to the extremely short pulse duration of the excimer laser, which has a diffusion length of the thermal wave L_T as described by Eq. (5.1):

$$L_T = \sqrt{D_{th}\tau} \qquad\qquad (5.1)$$

Where D_{th} is the thermal diffusivity and τ is the pulse duration. For the short pulse duration of the excimer laser, 25 ns and thermal diffusivity, D_{th} of 0.3–0.5 cm^2/s for nanostructure [95], the thermal diffusion length, L_T, was estimated to be ~ 1 μm. This explains why the laser interaction and damage was localized at the irradiated surface such that only a very thin melted and re-solidified layer was formed near the surface.

5.1.3 TEM and SAD analysis

To clarify the mechanism of phase transition in TNAs by laser annealing, the microstructures of TNAs along the tubes treated at 400 mJ/cm^2 fluence with 9000 shots were examined by TEM and SAD patterns. The TEM images and SAD patterns of one short TNAs segment (~1.2 μm in length) are shown in Figs. 5.5(a)-5.5(f). A full cross-section TEM image of TiO$_2$ nanotubes (Fig. 5.3(a)) shows that the TiO$_2$ nanotubes had a tube diameter of 50 nm with a tube wall thickness of 15 nm. Furthermore, the microstructure of the TNAs was examined by HRTEM as shown in Figs. 5.3(b) through 5.3(d). To be more specific, the top part of the nanotube segment (Fig. 5.3(b)) showed crystal lattice fringes with spacings of 3.52, 2.43, 2.37, 2.33 and 1.69 Å. Their corresponding SAD patterns (Fig. 5.3(e)) include a series of continuous Debye-Scherer rings, which are identified to the spacings of $d_{(101)}$, $d_{(103)}$, $d_{(004)}$, $d_{(112)}$, and $d_{(200)}$ of anatase TiO$_2$, respectively [96]. The HRTEM image for the middle part of the nanotube segment (Fig. 5.3(c)) showed that anatase crystalline structure was surrounded by amorphous structure. The HRTEM image (Fig. 5.3(d)) and the corresponding featureless SAD

pattern (Fig. 5.3(f)) for the bottom part of the nanotube segment clearly shows that this section was in fully amorphous phase. From SEM images and the TEM results of the microstructures along the nanotube, it is found that the phase transformation starts from the surface, and then extends downward to the middle part of the nanotube.

As a result, the temperature profile along the TiO_2 nanotubes during excimer laser pulse can be described by the one-dimensional heat conduction equation [97,98] in Eq. (5.2):

$$\frac{\partial T}{\partial t} = \frac{\alpha}{\rho Cp} I(z,t) + \frac{1}{\rho Cp} \frac{\partial}{\partial z}\left(k\frac{\partial T}{\partial z}\right) \tag{5.2}$$

Where $I(z,t) = I_o(t)(1-R)e^{-\alpha z}$ is the laser pulse intensity at depth z and time t. T, α, ρ, Cp, k and R are the temperature, the absorption coefficient at 248 nm, the density, the specific heat, the thermal conductivity and the reflectivity, respectively. From Eq. (5.2), the temperature profile is as a function of depth. In this study, the ordered nanotube arrays are expected to exhibit a strong anisotropic thermal transport behavior due to its high porosity structure. Strong anisotropic thermal conductivity has been reported for TiO_2 nanotube arrays [99]. The thermal conductivities in the tube-length direction and in the cross-tube direction are 0.617 and 0.077–0.102 $WK^{-1}m^{-1}$ for amorphous TNAs, 1.12 and 0.24 $WK^{-1}m^{-1}$ for anatase TNAs, respectively [99]. However, this thermal transport from top surface to the bottom still limited the crystallinity of the TNAs. Hence, in order to improve the crystallinity, a tilted mode design was carried out to analyze its effect on the structure and morphology of the TNAs in the following section.

5.2 ELA treatment of TNAs in a tilted mode

5.2.1 XRD

In order to improve the crystallinity in TNAs obtained by parallel mode, which is limited by the penetration depth of the laser, a tilted mode of irradiation onto TNAs at various angles from 30° to 85°, as illustrated in Fig. 5.4, was carried out for comparative study. Fig. 5.4 shows the XRD patterns of the TNAs laser-annealed in parallel mode and tilted mode at a fluence of 125 mJ/cm^2 and 9000 total shots, in addition to TNAs annealed at 400 °C for 1 hr under a conventional furnace anneal. For TiO$_2$ treated by ELA in a tilted mode of 30°, the intensities of anatase peaks A(101) and A(200) were higher compared to those of the parallel mode, but were still lower than those obtained by conventional furnace annealing. When the tilted angle was further increased to 85°, the intensity of the A(101) peak increased with increasing tilted angle and approached that obtained by furnace annealing. This indicated that the crystalinity of TNAs was significantly enhanced in the tilted mode.
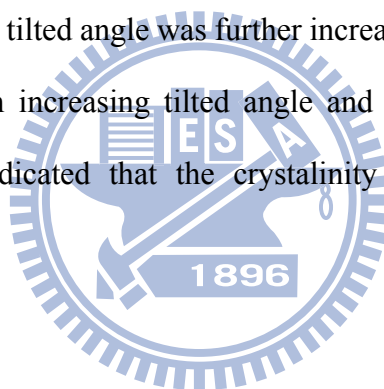
5.2.2 SEM

Fig. 5.5 illustrates the surface morphology of TNAs treated by ELA in (a) parallel mode and tilted mode: (b) 30°, (c) 75° and (d) 85° using a fluence of 125 mJ/cm^2 and 9000 total shots. For TNAs treated by ELA in parallel mode (Fig. 5.5(a)), a re-solidified layer was formed on the top of the nanotube arrays, as discussed in the previous section. In the parallel mode, 9000 shots laser pulses irradiated perpendicularly to the surface of the TNAs such that the top surface of the tubes accumulated a large amount of energy in a short duration, resulting in damage and melting. When TNAs were irradiated by the laser in tilted mode at tilted angles of 30°, 75° and 85° (Figs. 5.5(b) to 5.5(d)), the surface morphology of the TNAs was slightly affected by laser annealing. The damage on the surface was greatly reduced with increasing tilted angle. At a tilted angle of 85° (Fig.

5.5(d)), few tubes were broken and only a few scattered melted spots were formed on the surfaces of tubes. On the other hand, in the tilted mode, the middle part of the TNAs was irradiated by most of the laser beam. Hence, the surface morphology of TNAs was only slightly affected.

5.2.3 TEM

Finally, Figs. 5.6(a) to 5.6(f) show the TEM images and SAD patterns of TNAs annealed by the excimer laser with a tilted angle of 85° at a fluence of 125 mJ/cm^2 for a total of 9000 shots. A full cross-section TEM image of the TiO_2 nanotubes (Fig. 5.6(a)) showed that the morphology of TiO_2 still had a highly ordered nanotube structure of about 1.2 μm in length. On the other hand, the microstructure of TNAs was examined by HRTEM images and SAD patterns, as shown in Figs. 5.6(b) through 5.6(f). Small TiO_2 crystallites with a diameter of approximately ~15 nm were present in the tube walls. Furthermore, these crystallites were identified to be anatase TiO_2 by high resolution lattice image. Also, the electron diffraction patterns (Figs. 5.6(e) and 5.6(f)) has several continuous rings, corresponding to the spacings of $d_{(101)}$, $d_{(103)}$, $d_{(004)}$, $d_{(112)}$, and $d_{(200)}$ of anatase phase, respectively [96]. Compared to the microstructure of TNAs treated by ELA in parallel mode, ELA in tilted mode indeed significantly enhances the crystallinity of TNAs along the tube length direction.

5.3 ELA treatment vs. 400°C furnace annealing

Table 5.1 summarizes the XRD peak intensity ratio (I_A/I_{Ti}) of anatase (101) to Ti (101) for TNAs annealed in a conventional furnace anneal and ELA in parallel and tilted modes. For excimer laser annealing in parallel mode, the intensity of anatase (101) was 50% relative to the crystallinity of TNAs annealed by furnace annealing at 400°C for 1 hr. However, when tilted angle of 30° in tilted mode was used, the intensity of the anatase

phase was increased to 65% relative to that of furnace annealing. When the angle was further increased to 85°, the intensity of the anatase phase was close to 90% in comparison to furnace annealing. This means that ELA annealing of TNAs in the tilted mode can achieve crystallinity close to that of furnace annealing with reduced treatment time (15 mins).

Also, the percentage of anatase phase in the TNAs treated by ELA in tilted mode was higher than that in parallel mode. This contrasting result might be explained as follows. When TNAs were treated by the laser in parallel mode, the energy of the laser beam was transferred from the top to bottom of the TNAs. Therefore, the top of the tubes was transformed from amorphous to anatase or rutile, but the middle or bottom part of the tube underwent limited phase transformation because the laser energy could not reach such a depth, due to limited thermal conduction. However, in the tilted mode, the laser beam irradiated onto the middle part of the TNAs such that the heat could be conducted toward both the top and the bottom parts of the tubes. Furthermore, in the tilted mode, the area of the laser interaction energy zone increased with increasing tilted angle, α, according to the relation $L(\alpha) = L_o(\cos\alpha)^{-1}$ [100], where L_0 is the penetration depth in the parallel mode. When a tilted angle of 85° in tilted mode was used, the penetration depth was increased to about ten times relative to that of parallel mode. Therefore, the increased area of the laser interaction energy zone in the tilted mode accounts for its better effectiveness in energy transfer, heat conduction, and phase transformation into antase.

5.4 Summary

In this chapter, TiO$_2$ nanotube arrays (TNAs) with high aspect ratio (170:1) on Ti foil have been prepared by anodization method using NH$_4$F electrolyte. The structural and morphological transformation of TNAs treated by excimer laser annealing was investigated as a function of the laser fluence using parallel and tilted modes. In parallel mode, the morphology of TNAs showed the formation of the flower-like and re-solidified layer at a high fluence because the laser induced surface melting and coalescence. Also, the crystallinity of ELA-treated TNAs reached only about 50% relative to that of TNAs treated by furnace annealing at 400°C for 1 h. This can be attributed to short penetration depth and limited one-dimensional heat transport from the surface to the bottom under extremely short pulse duration (25 ns) of the excimer laser. When a tilted mode was used, the crystallinity of TNAs treated by ELA at 85° was increased to 90% relative to that by the furnace anneal. This can be attributed to the increased area of the laser energy interaction zone and better heat conduction to both ends of the TNAs

Table 5.1 The XRD peak intensity ratios of TNAs annealed in conventional furnace anneal at 400°C, 1 hr and excimer laser in parallel and tilted modes at a fluence of 125 mJ/cm^2 for a total of 9000 shots.

Annealing condition	Peak intensity ratio	
	$I_{A(101)}/I_{Ti(101)}$	Normalized to furnace anneal
Furnace anneal 400° C, 1 hr	0.907	100%
ELA, tilted mode, 85°	0.823	91%
ELA, tilted mode, 75°	0.804	88%
ELA, tilted mode, 30°	0.589	65%
ELA, parallel mode	0.471	50%
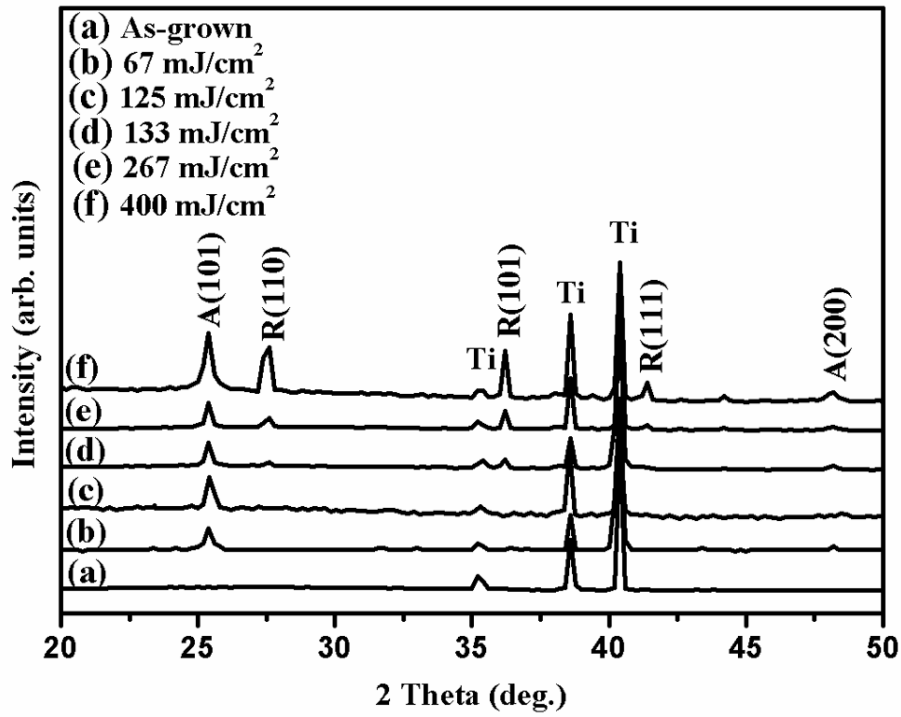
Figure 5.1 XRD patterns of the TNAs prepared by anodic oxidation in NH$_4$F solution (as-grown) and annealing by excimer laser with various fluences at 9000 shots.
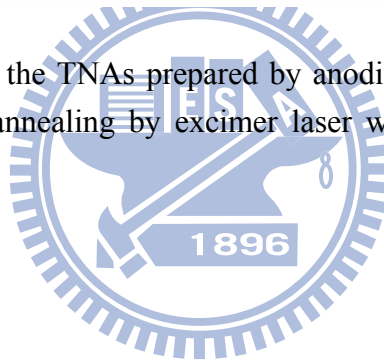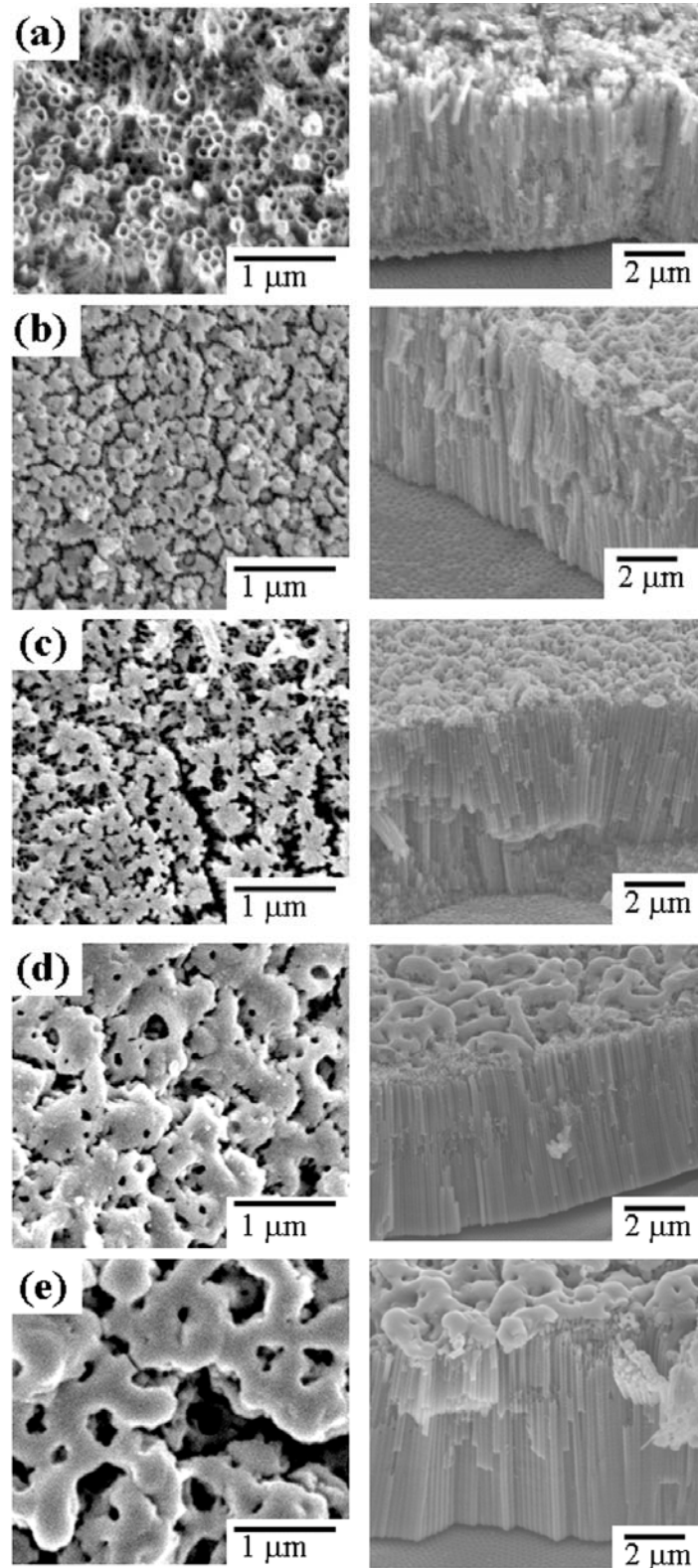
Figure 5.2 Surface and cross-section morphology of the TNAs annealing by excimer
laser with various fluences: (a) 67 mJc/m^2, (b) 125 mJ/cm^2, (c) 133 mJ/cm^2,
(d) 267 mJ/cm^2, and (e) 400 mJ/cm^2 at 9000 shots.
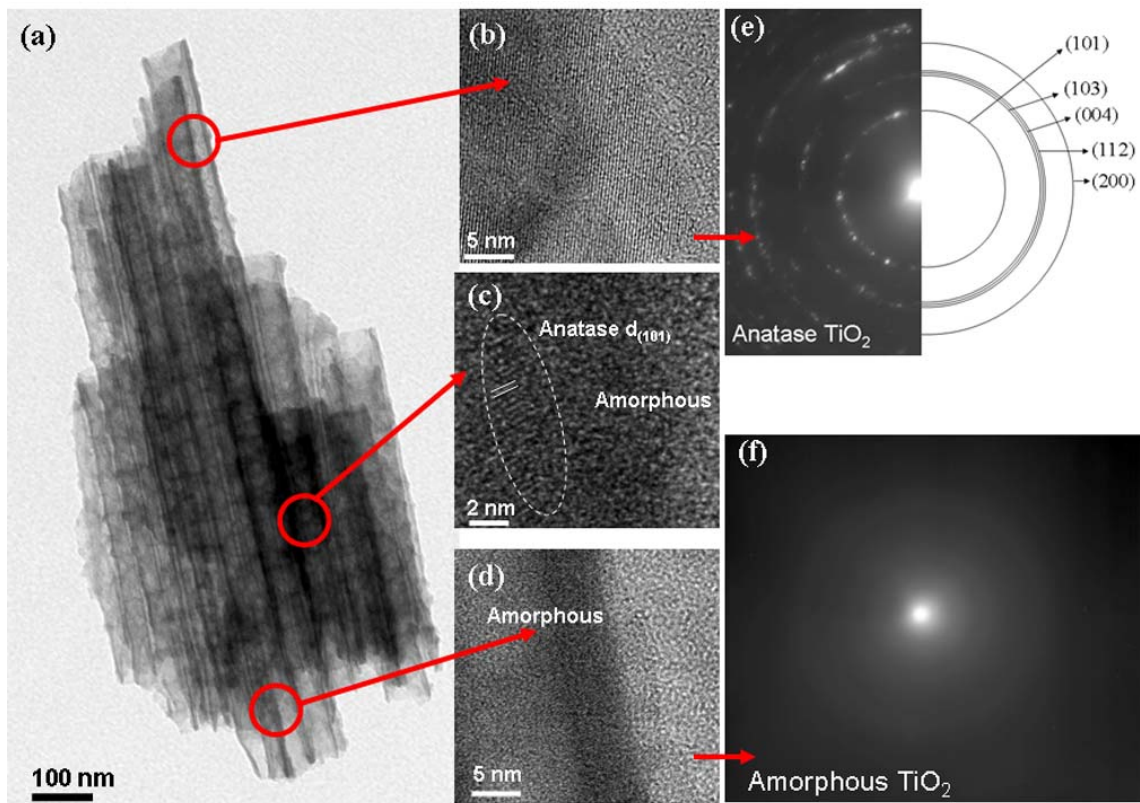
Figure 5.3 TEM images of the TNAs annealing by excimer laser at 400mJ/cm^2 for 9000 shots: (a) full cross-section, (b) the top part, (c) middle part (d) the bottom part of corss-section, and SAD patterns of (e) the top part and (f) the bottom part of cross-section.
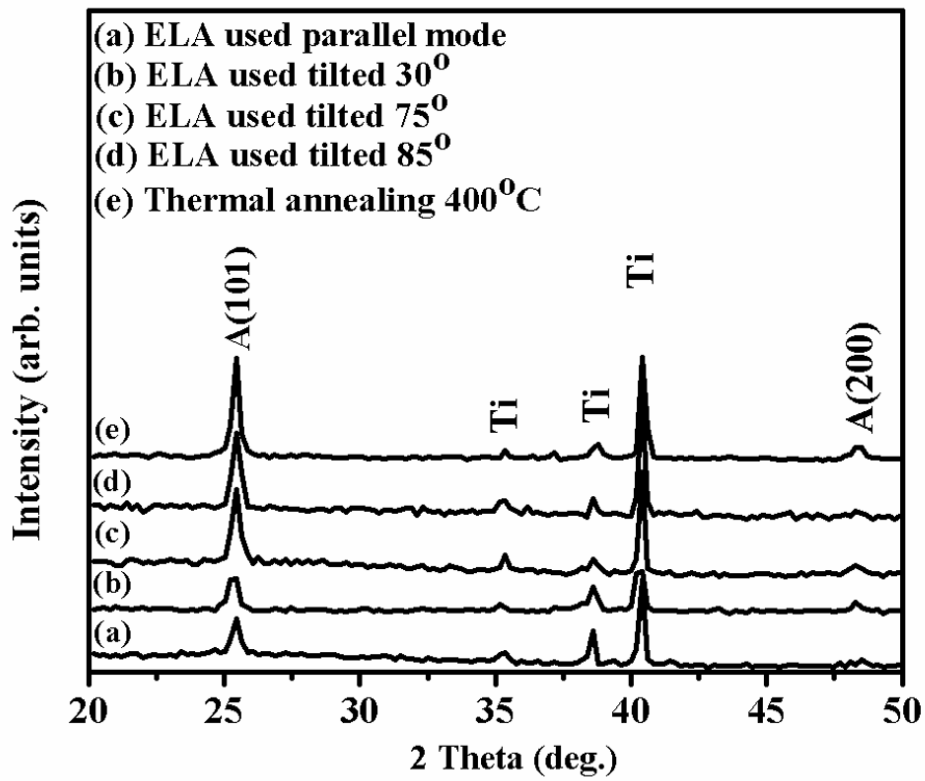
Figure 5.4 The XRD patterns of TNAs annealed by conventional furnace at 400 ^{o}C for 1
　　　hr and excimer laser in parallel mode and tilted mode at a fluence of
　　　125mJ/cm^2 for a total of 9000 shots.
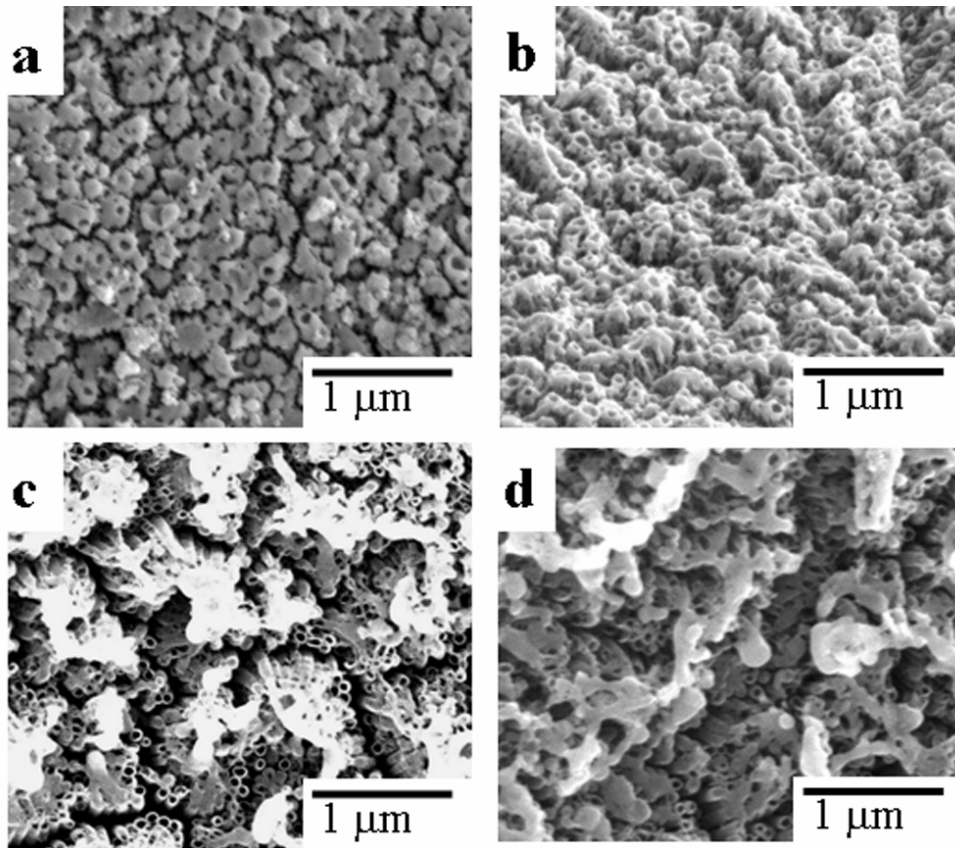
Figure 5.5 Surface morphologies of TNAs for laser annealing in (a) parallel mode, (b) 30° (c) 75°, and (d) 85° in tilted mode at a fluence of 125 mJ/cm^2 for a total of 9000 shots.
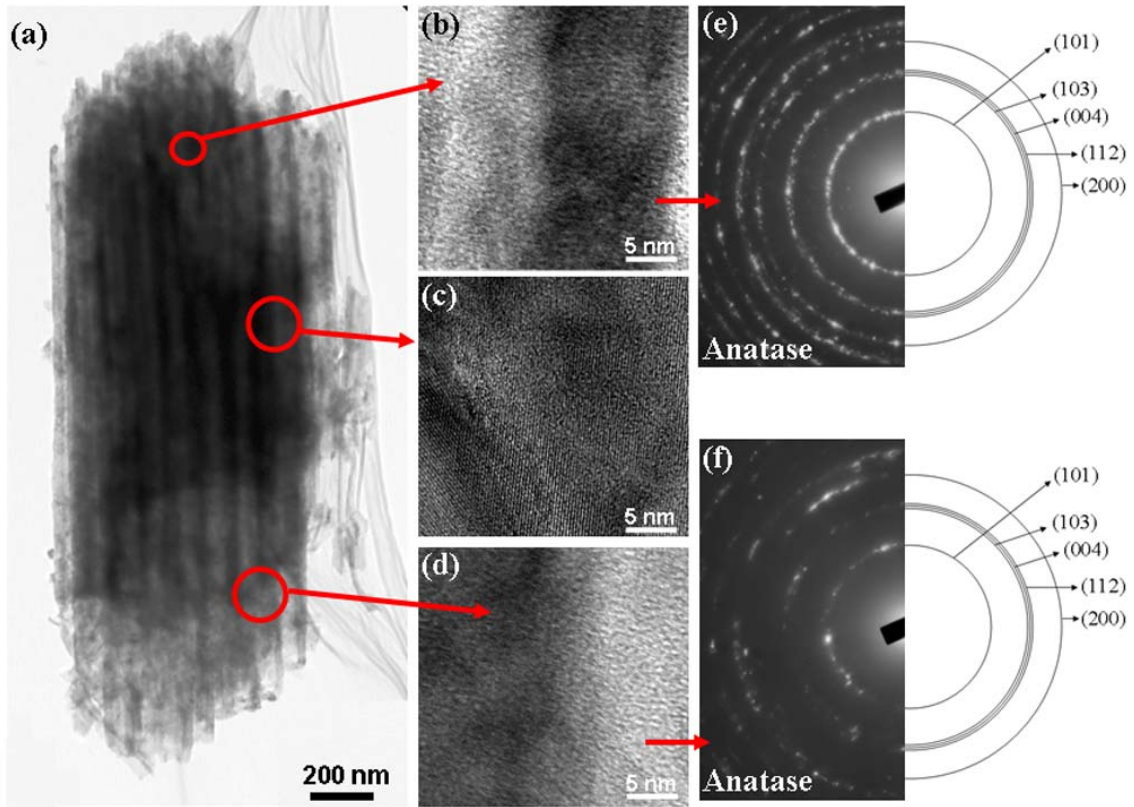
Figure 5.6 TEM images of TNAs annealing by excimer laser in 85° tilted mode at a fluence of 125 mJ/cm^2 for a total of 9000 shots: (a) full cross-section, (b) the top part, (c) middle part (d) the bottom part of corss-section, and SAD patterns of (e) the top part and (f) the bottom part of cross-section.

Chapter 6

TiO$_2$ nanowires on anodic TiO$_2$ nanotube arrays: formation mechanism and their photocatalytic performance

6.1 Influence of anodizing voltage

Figures 6.1(a)-(d) illustrate the SEM images of the TiO$_2$ films prepared by various anodizing voltages from 20 V to 80 V, in a 0.5 wt% NH$_4$F solution with a constant anodizing time of 1 h. At anodizing voltage of 20 V shown in Fig. 6.1(a), the surface morphology showed highly ordered TiO$_2$ nanotube arrays with a tube diameter (i.e. inner wall diameter) of 40 nm and a wall thickness of 20 nm. When the anodizing voltage was increased to 40V, instead of highly ordered TNAs, TNWs appeared on the top surface with a wire width ~50 nm. For the TiO$_2$ nanotubes beneath the TNWs, a diameter of 60 nm and a wall thickness of ~10 nm was observed. As the anodizing voltage was further increased to 60 V, the entire surface was covered by TNWs with a width ~20 nm on the TNAs with a diameter of 80 nm and a wall thickness of ~10 nm TNAs. When the anodizing voltage was raised to 80V, strikingly, there were no nanowires on the surface, only highly ordered TNAs with a diameter of ~110 nm.

6.2 Influence of anodizing time

In order to understand the formation mechanism of TNWs/TNAs, the evolution of TiO$_2$ film was observed for a fixed anodizing voltage of 40V and varied anodizing times, from 30 to 120 min. Figures 6.2(a)-(d) show the SEM images for the surface morphology of TiO$_2$ films prepared under a constant anodizing voltage of 40 V using an anodizing time of 30, 35, 38, and 40 min, respectively. For an anodizing time of 30 min, the length of the highly ordered TNAs structure was 12.2 μm, as shown in the inset of

72

Fig. 6.2(a); the TNAs structure possesses a tube diameter of 60 nm and a wall thickness of 18 nm. Up to 30 min, the steady-state growth rate of the TNAs length is approximately 0.4 μm/min. This suggests that high H^+ concentration is maintained at the pore bottom during chemical drilling[29] because the high-viscosity EG electrolyte limits the ionic diffusion of the electrolyte with a protective environment maintained along the pore walls and at the pore mouth during chemical drilling.

When the anodizing time was further increased to 35, 38, and 40 min as illustrated in Figs. 6.2(b) to 6.2(d), a gradual change of the surface morphology near the top of the TNAs was observed. As the treatment time was increased from 30 to 35 min, the wall thickness was reduced from 18 nm (Fig. 6.2(a)) to 12 nm (Fig. 6.2(b)) due to the high electrochemical etching rate near the top of the TNAs. However, near the intermediate section of nanotubes, the wall thickness of the TNAs remained the same, ~18 nm, as shown by the inset of Fig. 6.2(b). This implies that there was enhanced electrochemical etching occurs near the top of the nanotube mouths, relative to the tubes in the intermediate section. As the treatment time was further increased to 38 and 40 min, as illustrated in Figs. 6.2(c) and 6.2(d), the wall thickness became even thinner and the tubes started disintegrating in this transitional stage. After 45 min (Fig. 6.3(a1)), some of the TNAs near the top surface were broken up, along with the thinning of wall thickness down to about 10 nm. Further increasing the treatment time to 60 min, as illustrated by Fig. 6.3(b1), TNWs with a wire width of ~50 nm were found on the entire surface. The nanowires then fell down on the top of the TNAs when its length became too long (~2 μm). When the treatment time was increased up to 90 and 120 min (Figs. 6.3(c1) and 6.3(d1)), the TNWs completely covered on the top of the TNAs. The width of TNWs also decreased from 50 nm (after 60 min) down to ~30 nm (after 90 min), then to ~20 nm (after 120 min), due to electrochemical etching. Moreover, from the

cross-section images illustrated in the right column of Fig. 6.3(a2) to 6.3(d2), the individual thicknesses of TNWs and TNAs layers in the TNWs/TNAs structure showed a different trend after the emergence of nanowires. The structure of the TNWs/TNAs with an anodizing time of 45 min showed two different zones in the cross-section image. At 45 min, the top layer's (partially TNWs and mostly TNAs in the transitional stage) thickness was ~2 μm, and the thickness of the TNAs was ~10 μm. After 60 min, the structure collapsed into ~1 μm thickness of nanowires after splitting of the tubes, and the thickness of the TNAs maintained at 10 μm as shown in Fig. 6.3(b2). However, the thickness of TNWs did not change with time and remained at about 1 μm on the top surface. As the anodizing time was further increased to 90 and 120 min, the nanowire structure emerged upon further etching, whereas the length of the TNAs was increased to 11 μm (after 90 min; Fig. 6.3(c2)) and 12 μm (after 120 min; Fig. 6.3(d2)). A top-view of the TNWs, as illustrated in Fig. 6.3(d3), showed that the length of nanowires was 5-10 μm with excellent coverage.

Both the strength of the electric field and the processing time play important roles in the formation of TNWs/TNAs. Figure 6.4(a) summarizes the conditions of required anodizing voltage and processing time for forming TNWs/TNAs in a fixed electrolyte solution. For instance, TNWs/TNAs emerged after 120 min treatment at 30V, but only 30 min for anodizing voltage of 50-60V. To elucidate the influence of the electric field strength on the TNWs/TNAs, ion migration under electric field in the electrolyte shall be taken into consideration. In principle, the flux of ions in the presence of electric field can be expressed as :

$$J_i = -D_i \frac{\partial c_i}{\partial x} - u_i c_i E \tag{6.1}$$

where J_i is the flux of species i of concentration c_i in direction x, $\dfrac{\partial c_i}{\partial x}$ is the

concentration gradient, D_i is the diffusion coefficient, u_i is the mobility of species i, and

E is the electric field strength. Evidently, ion transport in the electrolyte is significantly

affected by field strength, since ion migration within the electric field is considerable in

comparison to the process of ion diffusion under a concentration gradient. According to

Eq. (6.1), higher field strength results in higher ion flux in the electrolyte. As a result,

under high field strength, the TNWs/TNAs structure formed in a shorter time. However,

TNWs emerges only under anodizing voltage of 30 to 60V with longer processing times

for lower voltages.

To understand the controlling factor(s) for the formation of nanowires onto TNAs,

the pore diameter and the wall thickness of TNAs top section prior to the emergence of

nanowires, as a function of voltage were quantified by SEM are shown in Fig. 4(b). For

cases with no TNWs formation, for example, at ≤20V or ≥80V, the tube diameter and

wall thickness were taken from TNAs after a processing time of 30 min. The pore

diameter of the TNAs mouth increased from 30 to 110 nm with increasing applied voltage

from 10 to 80V, which agreed with the reported results [101,102,103]. However, the wall

thickness of the TNAs mouths decreased from 20 nm to 8 nm as the applied potential was

raised from 10 to 80V. In particular, TNWs/TNAs occur only when the tube wall

thickness at the mouths is between 15 and 10 nm. From Figs. 6.4(a) and 6.4(b), it is clear

that if the applied voltage was too low, the lower dissolution rate could not break up TiO_2

tube wall, but retained the TNAs structure as function of time. In contrast, at specific

voltages, in which the wall thickness at the tube mouth is ~10 nm, the areas of thinner

wall near the top of the TNAs because of the high thickness non-uniformity from

roughness, would be etched through and form the nanowires. A detailed formation

mechanism will be proposed in the subsequent section. By contrary, if the anodizing voltage was too high together with a thin wall thickness of ~8 nm, TiO_2 tube wall of top section would be completely removed, resulting in shortened TiO_2 nanotube arrays without nanowires.

6.3 Formation mechanism of the TNWs/TNAs

Based on above results, TiO_2 nanowires are found to evolve and form on the top of the TNAs through several stages. Figures 6.5(a) to 6.5(d) show the schematic diagrams along with their corresponding surface morphology SEM images for four key stages in the TNWs/TNAs formation mechanism. First, as the anodic titanium oxide reaction began, the ordered TNAs was formed, resulting from the field-enhanced chemical drilling by a high H^+ concentration at the pore bottom of the tubes, in conjunction with a protective environment maintained along the pore walls by the highly viscous EG solution, as described in the previous section. As the anodic oxidation reaction proceeded, field-enhanced dissolution in the tube bottom still prevailed to further increase the aspect ratio (height/diameter) of the TNA at this stage, as illustrated in Fig. 6.5(a). However, the wall thickness near the tube mouth shown in Fig. 6.5(a), became smaller due to enhanced dissolution of TiO_2. In the EG/H_2O solution containing NH_4F electrolyte, the migration of F^- toward the electric field of the bottom electrode, is inhibited by the highly viscous solution. This results in F^- concentration much higher at the tube mouth than at the tube bottom [104]. With the presence of water in our case, the hydrogen ions further enhance the chemical dissolution reaction of the formed TiO_2 tube [105]:

$$TiO_2 + 6F^- + 4H^+ \rightarrow TiF_6^{2-} + 2H_2O \tag{6.2}$$

Therefore, the tube wall thickness near the tube mouth was thinner than the lower sections as illustrated in Fig. 6.5(a).

Meanwhile, the inner surface of the tubes was rough, as reported by Liu et al. [106], because mechanical stirring in the electrolyte bath was not used in this study. Thus, the inner tube diameter of the TNAs was not uniform, as schematically illustrated in the inset 1 of Fig. 6.5(b) and marked by arrows. Under a specific voltage and processing time conditions, in which the wall thickness at the tube mouth is < 10 nm, the areas of thinner wall thickness near the top of the TNAs would be etched through by the enhanced TiO_2 dissolution reaction as illustrated in inset 2. With increasing processing time, strings of through holes on the tubes in the top section of the TNAs, were formed from top to bottom, along the F^- ion migration direction under electric field, as illustrated in Fig. 6.5(b).

As the TiO_2 dissolution reaction continued over time, the strings of through holes on the tube wall would initiate and propagate downward, while the holes near the top expanded and became connected to split into nanowires, as illustrated in Fig. 6.5(c). With increasing anodizing time, the nanowires were further electrochemically etched, resulting in smooth wire edge and narrower wire width of nanowires. In addition, the nanowires would collapse onto the TNAs when its length is ~5-10 μm, as illustrated in Fig. 6.5(d). In summary, a strings-of-through-holes model is proposed, based on the enhanced TiO_2 dissolution reaction near the top section in conjunction with a threshold wall thickness of ~10 nm for forming nanowires and high thickness non-uniformity due to a lack of mechanical stirring. Four key stages in the TNWs/TNAs formation mechanism are: (a) thinning of the tube wall thickness with high roughness near the TNAs mouths, (b) forming strings of through holes in the top section of the TNAs, (c) splitting into nanowires, and (d) collapsing and further thinning of nanowires.

6.4 Photocatalytic reaction experiments

Our attention then shifted to the photocatalytic performance of TNWs/TNAs nanostructure. The effect of various TiO_2 morphologies including ordered TNAs and TNWs/TNAs on the photocatalytic degradation of methylene blue (MB) was examined and compared with that of TiO_2 film made of TiO_2 particles. In order to compare the photocatalytic performance of pure TNAs and TNWs/TNAs structures, we adjusted the process conditions (under mechanical stirring) to fabricate pure TNAs with diameters ranging from 40 to 100 nm with a total tube length or thickness of ~11 μm. Figure 6.6 shows the photodegradation of MB solution, C_t/C_o as a function of UV irradiation time for various anodized TiO_2 (TNAs and TNWs/TNAs) films and TiO_2 film of TiO_2 particles. It was found that MB degradation versus reaction time curves ($C_0=2.5\times10^{-5}$ M) follows a pseudo first-order kinetics as described by the Langmuir–Hinshelwood model [107]. Thus, the photodegradation rate of MB could be expressed by the following Eqs. (6.3) and (6.4):

$$C_t = C_0 e^{kt} \qquad (6.3)$$

$$\ln C_t/C_0 = kt \qquad (6.4)$$

where k is the apparent reaction rate constant, t is the irradiation time; C_0 and C_t are the initial concentration and the reaction concentration of MB. The reaction rate constants (k) were obtained from the experimental data using a linear regression. In all cases, correlation coefficients, R^2 values are all higher than 0.95, indicating that the Langmuir–Hinshelwood model can well describe the kinetics of MB degradation.

For TNAs structures with various tube diameters as shown in Fig. 6.6, the corresponding k values are 9.80×10^{-2} h^{-1}, 8.48×10^{-2} h^{-1}, 6.73×10^{-2} h^{-1} and 5.49×10^{-2}

h^{-1} for tube diameter of 40 nm, 60 nm, 80 nm, and 100 nm, respectively. A higher reaction rate was observed for TNAs with a smaller tube diameter at a fixed tube thickness. In comparison, for fixed TNAs with 60 nm tube diameter, the rate constant, k of 20 nm TNWs/60 nm TNAs is 12.54×10^{-2} h^{-1}, which is 48% higher than that of pure TNAs (8.40×10^{-2} h^{-1}). For fixed TNAs with 40 nm tube diameter, the rate constant, k of 20 nm TNWs/40nm TNAs is 13.05×10^{-2} h^{-1}, which is 33% higher than that of pure TNAs (9.80×10^{-2} h^{-1}). In short, the TNWs/TNAs film showed 33-48% higher photocatalytic activity than their corresponding pure TNAs.

The enhanced photocatalytic performance of TNWs/TNAs may be attributed to several factors such as increased surface area and reduced recombination, and others. Since the conventional Brunauer–Emmett–Teller (BET) method [108] is not suitable for measuring the surface area of various TiO$_2$ films, the dye desorption amount, an indicator of surface area, was measured by UV-visible spectrum. From the spectra data, the dye adsorption of a TiO$_2$ film could be calculated by comparing the light absorption intensity of dye-desorbed NaOH solution. In addition, Beer-Lambert law, as expressed by Eqs. (6.5) and (6.6), is applied to calculate the dye adsorption amount within various TiO$_2$ films.

$$T = \frac{I}{I_0} = 10^{-\alpha.l} = 10^{-\varepsilon.c.l} \tag{6.5}$$

$$A = -\log(\frac{I}{I_0}) = \varepsilon c l \tag{6.6}$$

where T is light transmittance, I is the absorption intensity, α is the absorption coefficient, l is the sample thickness, c is the concentration, ε is the extinction coefficient, and A is light absorption.

The absorbance intensity at 515 nm wavelength of a reference solution with dye concentration 8×10^{-5} M was 0.521. Using Eq. 6, the concentration of the solution, i.e. the dye adsorption on TiO$_2$ films, can be obtained by taking the hybrid film thickness (12 μm) into account. Fig. 6.7 shows the UV-visible spectra of the dye desorbed to NaOH solutions for TNAs, TNWs/TNAs, and TiO$_2$ nanoparticle films. In addition, the calculated dye adsorption, and reaction rate constants (k) of various TiO$_2$ films are summarized in Table 6.1. From Fig. 6.7 and Table 6.1, the dye adsorption of various pure TNAs films shows that a smaller tube diameter yields higher adsorption intensity. This means that TNA with a smaller tube diameter possesses has a higher surface area, which results in enhanced photocatalytic efficiency. For TNWs/TNAs films, the adsorption intensity, i.e. surface area, is higher than that for corresponding TNAs film. It is believed that the large surface area of the TiO$_2$ film enhances the adsorption of pollutants and enables light harvesting with a higher amount of photo-generated charge [109]. For pure TNAs, the difference in surface area comes from different tube density of anodic TNAs films. As the anodizing voltage increased, the tube density decreased with increasing tube diameter. In turn, the amount of dye adsorption decreased, leading to a reduced photocatalytic efficiency.

Meanwhile TNWs/TNAs structure had a higher photocatalytic efficiency than pure TNAs, which can be also attributed to the higher surface area of the nanowires. Dye adsorption data (Fig. 6.7) shows that TNWs/TNAs had higher adsorption intensity. Therefore, the congregation of the bundled nanowires connected to the nanotube mouths had a higher surface area than the nanotubes. Conversely, compared the change percentage between dye adsorption data and reaction rate constants, all the TNAs and TNWs/TNA films get higher reaction rate than dye adsorption data. This may be due to the fact that not only surface area, but also charge transport or reduced recombination

may also affect the photocatalytic performance, because the directly connected 1D nanostructures of the TNAs and TNWs/TNA may improve the charge-collection efficiency by promoting faster transport and slower recombination. This was helpful for faster transport and slower recombination to the random transport path in nanoparticles [64]. Overall, the photocatalytic performance (k value=13.05×10^{-2} h^{-1}) of TNWs/TNA on a Ti plate used in this study has achieved a very high efficiency, close to that of TiO$_2$ film (k value=14.38×10^{-2} h^{-1}). However, photocatalysis of pollutants in an immobilized film form, such as TNAs or TNWs/TNAs hybrid structure, is more practical than that in a TiO$_2$ powdery form. It is believed that the performance can be further improved by optimizing the width and density of the nanowire for a fixed TNAs structure.

6.5 Summary

In summary, we have demonstrated one-step process for the formation of TNWs/TNAs structure by anodization of Ti foils in a mixture of ethylene glycol and water containing NH_4F electrolyte without mechanical stirring. A formation mechanism for TNWs/TNAs is proposed and examined by changing the anodizing time and voltage. The evolution of TNWs/TNAs growth first involves thinning the tube wall thickness with high roughness and forming strings of through holes in the top section of the TNAs, due to enhanced dissolution of TiO_2 by the high F^- concentration and presence of H^+ from water. Then the strings of through holes on the tube wall initiate and propagate downward. Finally, the holes near the top expand and connect to split into nanowires. The TNWs/TNAs demonstrate superior photocatalytic ability, because of the congregation of the bundled nanowires connected to the nanotube mouths, which increases the surface area, and the TNWs directly connected on nanotubes gains an advantage to retard the charge recombination of the electron and hole pairs.
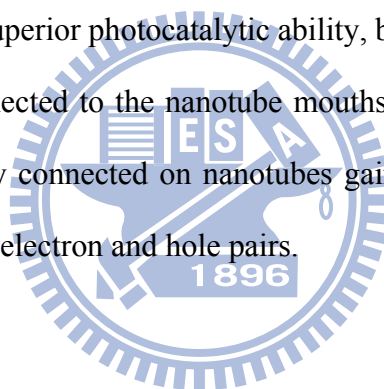
Table 6.1 Dye adsorption, reaction rate constants (k), and change percentage of various TiO$_2$ films.

TiO$_2$ film	Dye Adsorption ($\times 10^{-8}$ mol/cm^2)	change % relative to nanoparticles	reaction rate constants, k ($\times 10^{-2}$ h^{-1})	change % relative to nanoparticles
100 nm TNAs	1.22	29%	5.49	38%
80 nm TNAs	1.65	39%	6.73	47%
60 nm TNAs	2.33	55%	8.48	59%
40 nm TNAs	2.72	64%	9.80	68%
60 nm TNAs/ 20 nm TNWs	3.21	76%	12.54	87%
40 nm TNAs/ 20 nm TNWs	3.58	85%	13.05	91%
TiO$_2$ nanoparticles	4.22	100%	14.38	100%
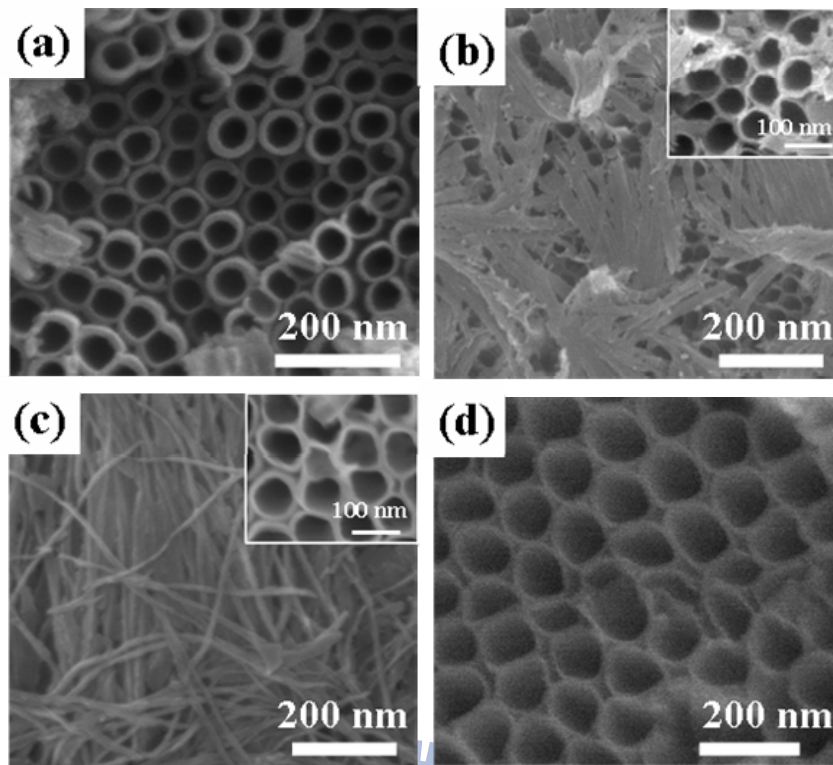
Figure 6.1 Surface morphology of the TiO$_2$ films prepared by anodic oxidation under different anodizing voltages: (a) 20 V, (b) 40 V, (c) 60 V, and (d) 80 V, with a constant anodizing time of 1 h.
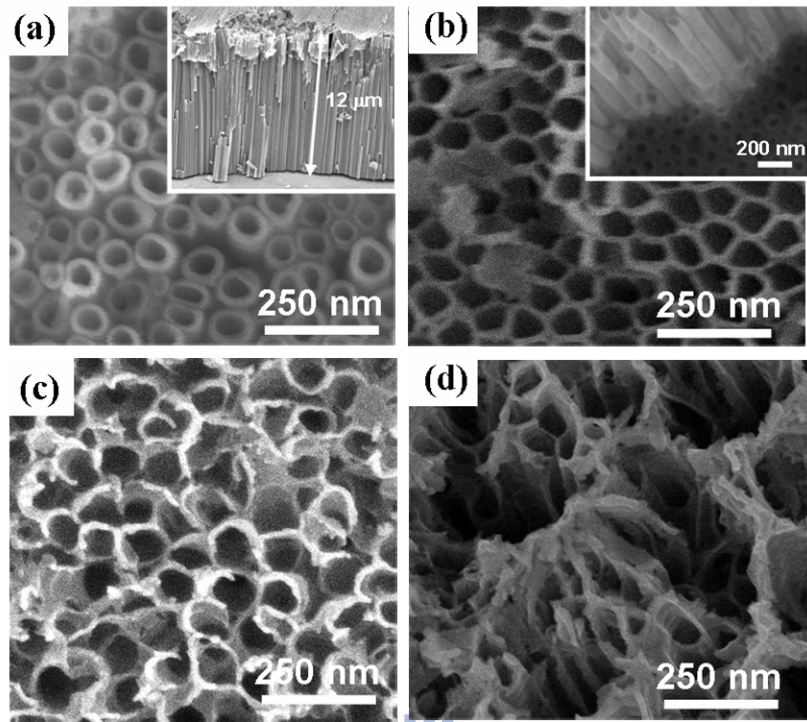
Figure 6.2 Surface morphology of the TiO$_2$ films prepared by anodic oxidation under
different anodizing time: (a) 30 min, (b) 35 min, (c) 38 min, and (d) 40 min,
with a constant anodizing voltage of 40 V.
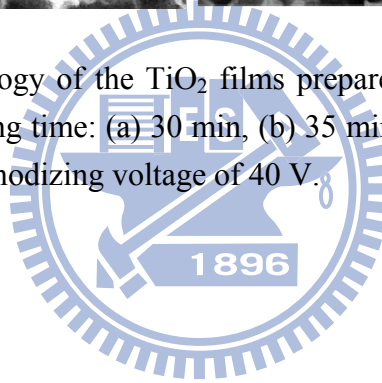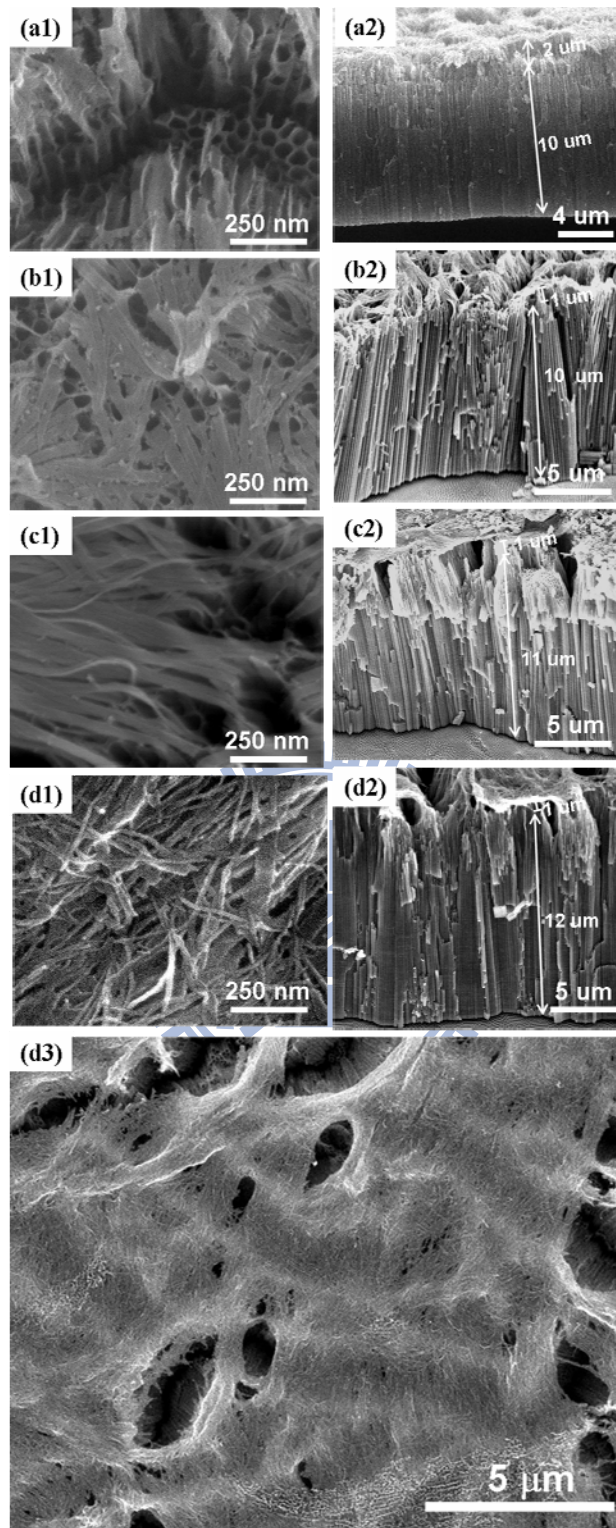
Figure 6.3 Surface (1) and cross-section (2) morphologies of the TiO_2 films prepared by anodic oxidation at different anodizing time: (a) 45 min, (b) 60 min, (c) 90 min, and (d) 120 min, with a constant anodizing voltage of 40 V; (d3) surface morphology at low magnification.
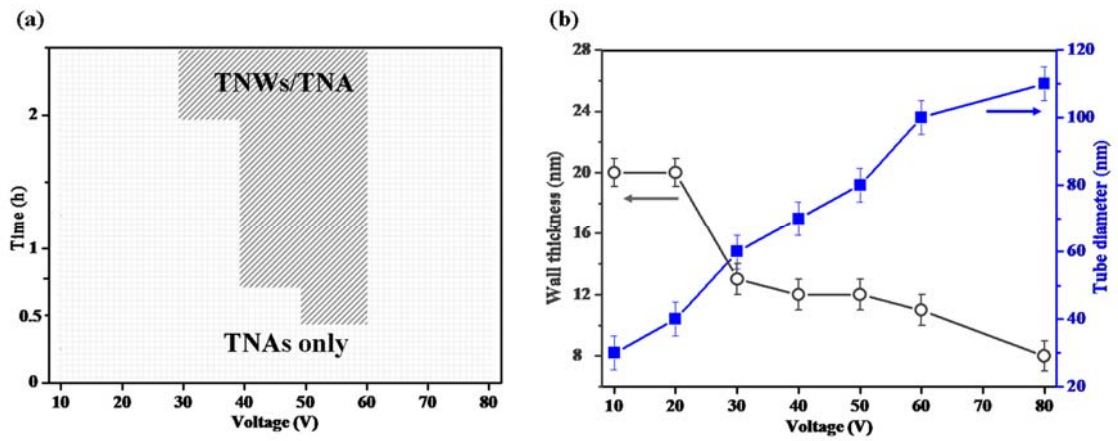
Figure 6.4 (a) Conditions of required anodizing voltage and processing time (shaded zone) for forming TNWs/TNAs. (b) The pore diameter and wall thickness of TNAs top section prior to the emergence of nanowires, as a function of voltage. For cases without TNWs formation, a processing time of 30 min was used.
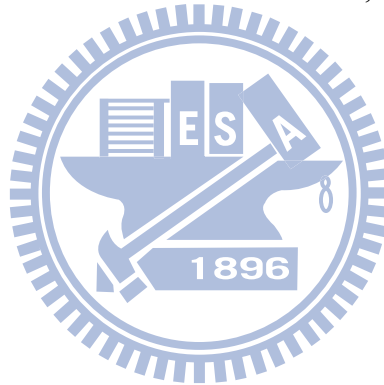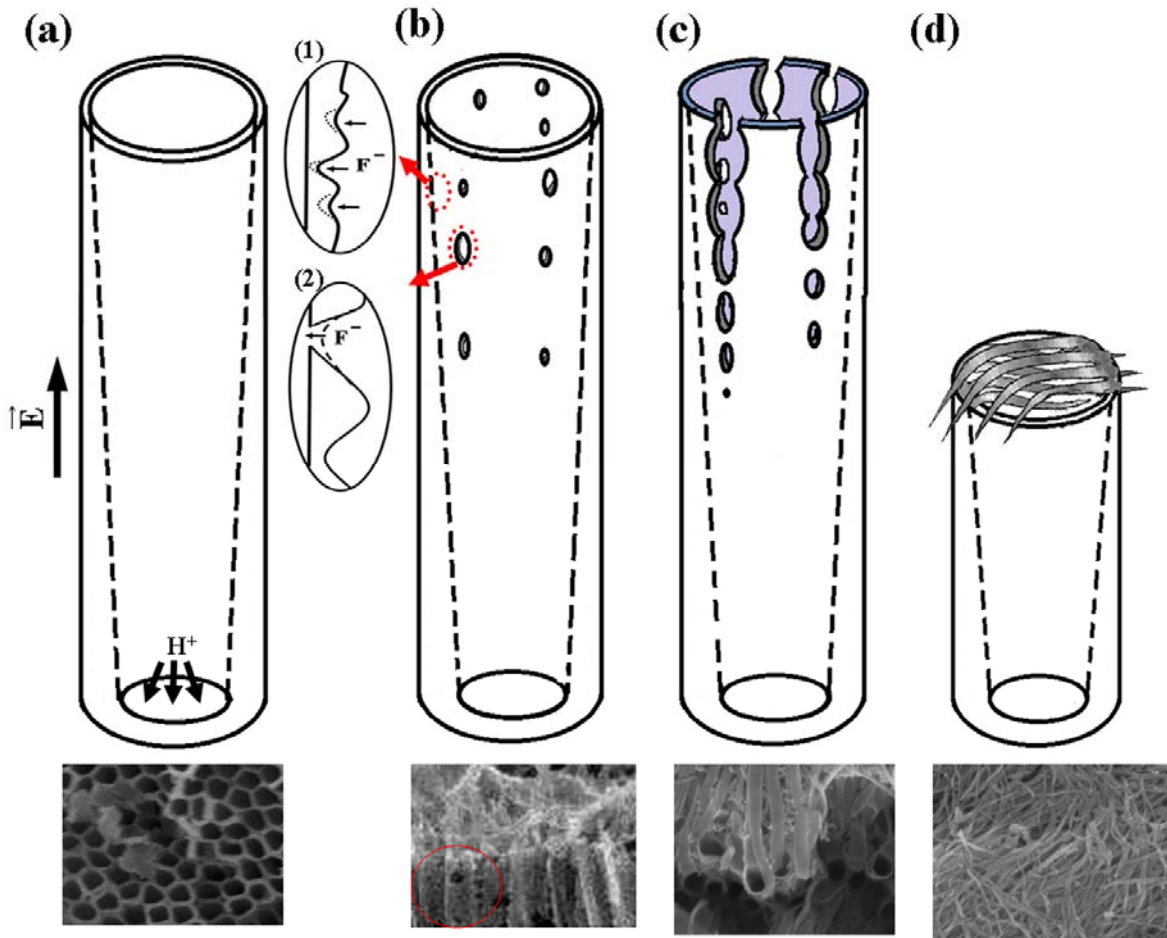
Figure 6.5 Schematic diagrams along with their corresponding surface morphology SEM images for four key stages in the TNWs/TNAs formation mechanism: (a) thinning the tube wall thickness with high roughness near the TNAs mouths, (b) forming strings of through holes in the top section of TNAs, (c) splitting into nanowires, and (d) collapsing and further thinning of nanowires.
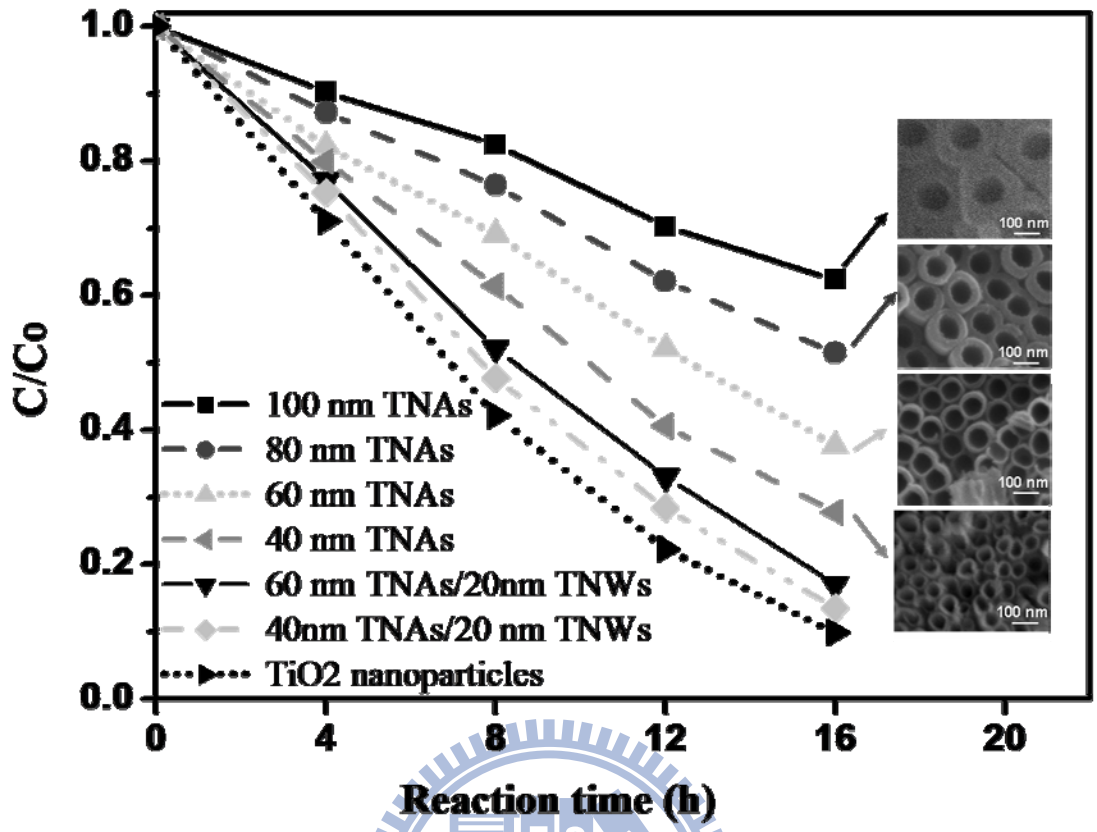
Figure 6.6 Photocatalytic degradation of MB under UV light irradiation, (C/Co) vs. reaction time plots for various TNAs, TNWs/TNAs, and TiO$_2$ nanoparticles films.
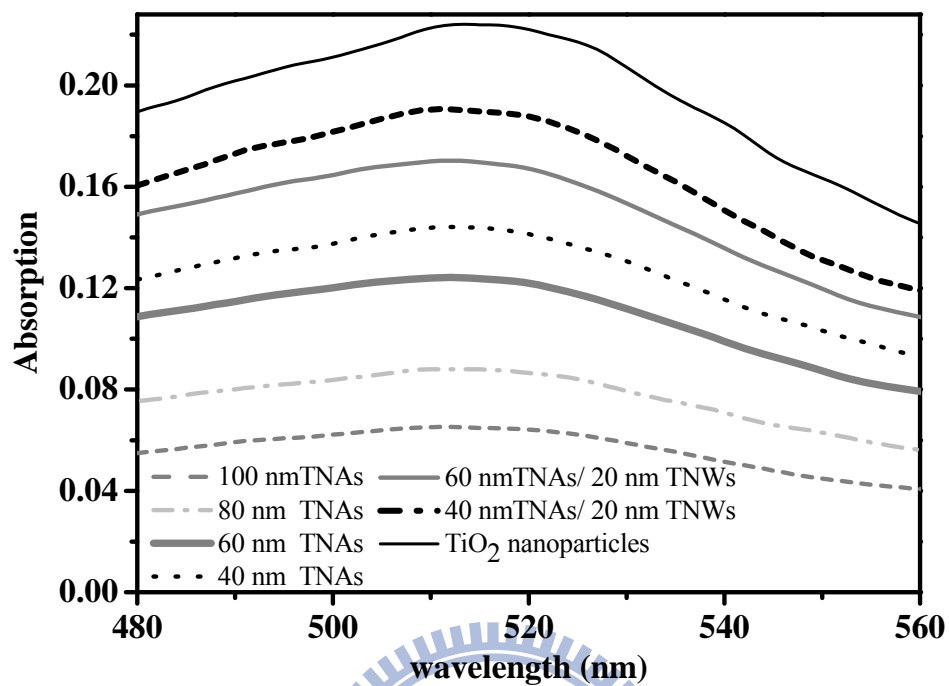
Figure 6.7 UV-visible spectra of the desorbed dye from the solution of various TNAs, TNWs/TNAs, and TiO$_2$ nanoparticles films.

Chapter 7

Conclusion

This study demonstrates the TNAs and TiO$_2$ hybrid structure prepared by electrochemical anodization, and furthermore approach some photocatalytic applications of these materials. Meanwhile, appropriate fast and low-temperature annealing process had been optimized for the high crystallinity TiO$_2$.

First, the evolution of microstructure and composition of TNAs fabricated with HF and NH$_4$F electrolytes as a function of annealing temperature up to 400 ^{o}C was investigated and compared using XRD, SEM, and XANES. Results showed that TiO$_2$ nanotube arrays grown in HF electrolyte contained 90% amorphous TiO$_2$ and 10% lower oxidation states of titanium from Ti^{2+} (TiO) and Ti^{3+} (Ti$_2$O$_3$) cations. After annealing at 400°C, TiO$_2$ nanotube arrays underwent charge transfer and phase transformation to 93% anatase phase, 6% amorphous TiO$_2$, and 1% suboxides. In contrast, as-grown TiO$_2$ nanotube arrays using NH$_4$F electrolyte possessed less amorphous TiO$_2$ (82%) but more suboxides (18%) due to lower oxygen ion formation from scanty 1wt% H$_2$O addition. Its onset temperature of phase transformation was found to be higher than TiO$_2$ nanotube arrays prepared by HF solution. Moreover, when annealed to 400°C, the crystallinity of TiO$_2$ nanotube arrays increased only to 86% for the anatase phase. The lower anatase phase could be attributed to the formation of (NH$_4$)$_2$TiF$_6$ type compounds presumably formed by the reaction of TiF$_6$$^{2-}$ and NH$_4$$^+$ ions dissociated from NH$_4$F.

On the other hand, the structural and morphological transformations of TiO$_2$ nanotube arrays (TNAs) treated by excimer laser annealing (ELA) were investigated as a function of the laser fluence using parallel and tilted modes. Results showed that the

crystallinity of the ELA-treated TNAs reached only about 50% relative to that of TNAs treated by furnace anneal at 400°C for 1 hr. The phase transformation starts from the top surface of the TNAs with surface damage resulting from short penetration depth and limited one-dimensional heat transport from the surface to the bottom under extremely short pulse duration (25 ns) of the excimer laser. When a tilted mode was used, the crystallinity of TNAs treated by ELA at 85° was increased to 90% relative to that by the furnace anneal. This can be attributed to the increased area of the laser energy interaction zone and better heat conduction to both ends of the TNAs.

Furthermore, TiO$_2$ nanowires connected directly with TiO$_2$ nanotubes arrays (TNWs/TNAs) for in photocatalysis application were successfully fabricated with a mixture of ethylene glycol and water containing NH$_4$F electrolyte using a one-step method. The morphology of TNWs/TNAs structure was investigated by changing the anodizing voltage and time to elucidate its formation mechanism. The evolution of TNWs results from the splitting on the top of nanotubes into nanograss, then into nanowires because of the high electric field near the top formed by high F$^-$ ion concentration built up by the high viscous electrolyte in the top of TNAs. For photocatalytic application, TNWs/TNAs film showed the best photocatalysis performance compared to regular TNAs due to higher surface area. Moreover, TNWs/TNAs film (20 nm wire/40 nm pore diameter) achieved comparable performance to that of TiO$_2$ nanoparticles.

References

[1] A. Fujishima and K. Honda, *Nature,* **238**, 37 (1972)

[2] A. Ghicov, H. Tsuchiya, R. Hahn, J. M. Macak, A. G. Mũnoz, and P. Schmuki, *Electrochem. Commun.*, **8**, 528 (2006).

[3] R. Hahn, A. Ghicov, H. Tsuchiya, J. M. Macak, A. G. Mũnoz, and P. Schmuki, *Phys. Status Solidi A*, **204**, 1281 (2007).

[4] J. Papp, H. S. Shen, R. Kershaw, K. Dwight, and A. Wold, *Chem. Mater.*, **5**, 284 (1993).

[5] J. M. Macak, M. Zlamal, J. Krysa, and P. Schmuki, *Small*, **3**, 300 (2007).

[6] M. A. Fox, and M. T. Dulay, *Chem. Rev.* **93**, 341 (1993)

[7] C. Garzella, E. Comini, E. Tempesti, C. Frigeri, and G. Sberveglieri, *Sens. Actuators B*, **68**, 189 (2000).

[8] M. Paulose, O. K. Varghese, G. K. Mor, C. A. Grimes, and K. G. Ong, *Nanotechnology*, **17**, 398 (2006).

[9] B.O'Regan, and M. Grätzel, *Nature* **353**, 737 (1991)

[10] T. Stergiopoulos, A. Ghicov, V. Likodimos, D. S. Tsoukleris, J. Kunze, P. Schmuki, and P. Falaras, *Nanotechnology*, **19**, 235602 (2008).

[11] J. R. Jennings, A. Ghicov, L. M. Peter, P. Schmuki, and A. B. Walker, *J. Am. Chem. Soc.*, **130**, 13364 (2008).

[12] Y. L. Li and T. Ishigaki, *J. Cryst. Growth*, **242**, 511 (2002).

[13] M. R. Hoffmann, S. T. Martin, W. Choi, and D. W. Bahnemann, *Chem. Rev.*, **95**, 69 (1995).

[14] L. Gao and Q. Zhang, *Scripta mater.*, **44**, 1195 (2001).

[15] J. Ovenstone, *J. Mater. Sci.*, **36**, 1325 (2001).

[16] J. G. Yu, H. G. Yu, B. Cheng, X. J. Zhao, J. C. Yu, and W. K. Ho, *Phys. Chem. B*, **107**, 13871 (2003).

[17] H. Kominami, J. I. Kato, S. Y. Murakami, Y. Ishii, M. Kohno, K. I. Yabutani, T. Yamamoto, Y. Kera, M. Inoue, T. Inui, and B. Ohtani, *Catal. Today,* **84**, 181 (2003).

[18] N. G. Park, J. van de Lagemaat, and A. J. Frank. *J. Phys. Chem. B*, **104**, 8989 (2000).

[19] Y. F. Joya and Z. Liu, *Scr. Mater.*, **60** (2009) 467.

[20] Q. Fang, J. Y. Zhang, Z. M. Wang, J. X. Wu, B. J. O'Sullivan, P. K. Hurley, T. L. Leedham, H. Davies, M. A. Audier, C. Jimenez, J. P. Senateur, and I. W. Boyd, *Thin Solid Films*, **428**, 248 (2003).

[21] C. Gopalakrishnan, K. R. Ganesh, S. Ramaswamy, and K. Jeganathan, *Mater. Lett.*, **65**,1941 (2011).

[22] H. Pan, S. H. Ko, N. Misra, and C. P. Grigoropoulos, *Appl. Phys. Lett.*, **94**, 071117 (2009).

[23] P. Mitrev, G. Benvenuti, P. Hofman, A. Smirnov, and N. Kaliteevskaya, *Tech. Phys. Lett.*, **31**, 908 (2005).

[24] G. K. Mor, O. K. Varghese, M. Paulose, K. Shankar, and C. A. Grimes, *Sol. Energy Mater. Sol. Cells*, **90**, 2011 (2006).

[25] I. Turkevych, Y. Pihosh, K. Hara, Z. S. Wang, and M. Kondo *Jpn. J. Appl. Phys.* **48**, 06FE02 (2009).

[26] Y. Alivov and Z. Y. Fan, *Appl. Phys. Lett.*, **95**, 063504 (2009).

[27] G. K. Mor, K. Shankar, M. Paulose, O. K. Varghese, and C.A. Grimes, *Nano Lett.* **6**, 215 (2006).

[28] V. Zwilling, E. D. Ceretti, A. B. Forveille, D. David, M. Y. Perrin, and M. Aucouturier, *Surf. Interface Anal.*, **27**, 629 (1999).

[29] J. M. Macak, H. Tsuchiya, and P. Schmuki, *Angew. Chem. Int. Ed.*, **44**, 2100 (2005).

[30] J. M. Macak, H. Tsuchiya, L. Taveira, S. Aldabergerova, and P. Schmuki, *Angew. Chem. Int. Ed.*, **44**, 7463 (2005).

[31] J. H. Lim and J. Choi, *Small*, **3**, 1504 (2007).

[32] Y. Wang, H. X. Yang, and H. Xu, *Mater. Lett.*, **64**, 164 (2010).

[33] V. S. Lusvardi, M. A. Barteau, J. G. Chen, J. Eng, Jr., B. Frühberger, and A. Teplyakov, *Surf. Sci.*, **397**, 237 (1998).

[34] M. Yoshiya, I. Tanaka,K. Kaneko, and H. J. Adachi, *Phys. Condes. Matter.*, **11**, 3217 (1999).

[35] S. O. Kucheyev, T. V. Buuren, T. F. Baumann, J. H. Satcher Jr., T.M. Willey, R.W. Meulenberg, T. E. Felter, J. F. Poco, S. A. Gammon, and L. J. Terminello, *Phys. Rev. B*, **69**, 245102 (2004).

[36] U. Diebold, *Surf. Sci. Report*, **48**, 53 (2003).

[37] S. D. Mo. and W. Y. Ching, *Phys. Rev. B*, **51**,13023 (1995).

[38] Z. H. Zhou, W. K. Li and Z. Q. Chen, *Key Eng Mater.*, **1462**, 368 (2008).

[39] J. G. Li, T. Ishigaki, and X. Sun, *J. Phys. Chem. C*, **111**, 4969 (2007)

[40] S. Lee, C. Jeon, and Y. Park, *Chem Mater.*, **16**, 4292 (2004).

[41] S. Liu and K. Huang, *Sol. Energy Mater. Sol. Cell.*, **85**, 125 (2005).

[42] Y. Chen, J. C. Crittenden, S. Hackney, L. Sutter, and D. W. Hand, *EnViron. Sci. Technol.*, **39**, 1201 (2005).

[43] S. K. Pradhan, P. J. Reucroft, F. Yang, and A. Dozier, *J. Cryst. Growth*, **256**, 83 (2003).

[44] M. Miyauchi, H. Tokudome, Y. Toda, T. Kamiya, and H. Hosono, *Appl Phys Lett.*, **89**, 043114 (2006).

[45] T. Kasuga, M. Hiramatsu, A. Hoson, T. Sekino, and K. Niihara, *Langmuir*, **14**, 3160 (1998).

[46] D. Gong, C. A. Grimes, O. K. Varghese, W. Hu, R. S. Singh, Z. Chen, and E. C. Dickey, *J. Mater. Res.*, **16**, 3331 (2001).

[47] H. Tsuchiya, J. M. Macak, A. Ghicov, L. Taveira, and P. Schmuki, *Corr. Sci.*, **47**, 3324 (2005).

[48] J. M. Macak and P. Schmuki, *Electrochim. Acta*, **52**, 1258 (2006).

[49] J. M. Macak, K. Sirotna, and P. Schmuki, *Electrochim. Acta*, **50**, 3679 (2005).

[50] Q. Cai, M. Paulose, O.K. Varghese, and C.A. Grimes, *J. Mater. Res.*, **20**, 230 (2005).

[51] G. K. Mor, O. K. Varghese, M. Paulose, K. Shankar, and C. A. Grimes, *Mater. Res. Soc. Symp. Proc.*, **836** ,L1.9.1 (2005).

[52] M. Paulose, O. K. Varghese, K. Shankar, G. K. Mor, and C. A. Grimes, *Mater. Res. Soc. Symp. Proc.*, **837** ,N3.13.1 (2005)

[53] M. Paulose, K. Shankar, S. Yoriya, H. E. Prakasam, O. K. Varghese, G. K. Mor, T. J. Latempa, A. Fitzgerald, and C. A. Grimes, *J. Phys. Chem. B*, **110**, 16179 (2006)

[54] H. E. Prakasam, K. Shankar, M. Paulose, O. K. Varghese, and C. A. Grimes, *J. Phys. Chem. C*, **111**, 7235 (2007).

[55] K. Shankar, G. K. Mor, H. E. Prakasam, S. Yoriya, M. Paulose, O. K. Varghese and C. A. Grimes, *Nanotechnology*, **18**, 065707 (2007).

[56] G. E. Thomson, *Thin Solid Film*, **297**, 192 (1997).

[57] H. Liu, L. Tao, and W. Shen, *Nanotechnology*, **22**, 155603 (2011).

[58] G. K. Mor, K. Shankar, M. Paulose, O. K. Varghese, and C. A. Grimes, *Nano. Lett.*, **5**, 191 (2005).

[59] C. H. Lin, C. H. Lee, J. H. Chao, C. Y. Kuo, Y. C. Cheng, W. N. Huang, H. W. Chang, Y. M. Huang, and M. K. Shih, *Catal. Lett.*, **98**, 61 (2004).

[60] H. Tokudome and M. Miyauchi, *Chem. Lett.*, **33**, 1108 (2004).

[61] E. Comini, G. Faglia, G. Sberveglieri, Z. Pan, and Z. L. Wang, *Appl. Phys. Lett.*, **81**, 1869 (2002).

[62] O. K. Varghese, D. Gong, M. Paulose, K. G. Ong, and C. A. Grimes, *Sens. Actuators B*, **93**, 338 (2003).

[63] H. J. Ryu, T. Sugiura, T. Yoshida, and H. Minoura, *Trans. Mater. Res. Soc. Japan*, **27**, 695 (2002).

[64] K. Zhu, N.R. Neale, A. Miedaner, and A. J. Frank, *Nano Lett.*, **7**, 69 (2007).

[65] H. Parala, A. Devi, R. Bhakta, and R. A. Fischer, *J. Mater. Chem.*, **12**, 1625 (2002).

[66] H. D. Jang, S. K. Kim, and S. J. Kim, *Journal of Nanoparticle Research*, **3**, 141 (2001).

[67] K. Y. Jung, S. B. Park, and S. K. Ihm, *Appl. Catal., A*, **224**, 229 (2002).

[68] M. Gratzel, *J. Photochem. Photobiol., A*, **164**, 3 (2004).

[69] D. J. Yang, H. Park, S. J. Cho, H.G. Kim, and W.Y. Choi, *J. Phys. Chem. Solids*, **69**, 1272 (2008).

[70] M. V. Allmen, Laser and Electron Beam Processing of Materials, Academic Press, New York, (1980).

[71] G. E. Wood, Melting Mode of Pulsed Laser Processing, Academic Press, New York, (1984).

[72] J. F. Ready, Effects of High Power Laser Radiation, Academic Press, New York, (1971).

[73] H. Kurz, *Mater. Res. Soc. Symp. Proc*., **74**, 3 (1987).

[74] J. W. Galvin and P. S. Peercy, *Appl. Phys. Lett.*, **46**, 644 (1985).

[75] C. P. Grigoropoulos, A. A. Rostami, X. Xu, S. L. Taylor, and H. K. Park, *Int. J. Heat Mass Transfer*, **36**, 1219 (1993).

[76] R. Ishihara, W-C. Yeh, T. Hattori, and M. Matsumura, *Jpn. J. Appl. Phys.*, **34**, 1759 (1995).

[77] S. C. Chung, C. I. Chen, P. C. Tseng, H. F. Lin, T. E. Dann, Y. F. Song, L. R. Huang, C. C. Chen, J. M. Chuang, K. L. Tsang, and C. N .Chang, *Rev. Sci. Instrum.*, **66**, 1655 (1995).

[78] F. M. F. De Groot, J. Faber, J. J. M. Michiels, M. T. Czyzyk, M. Abbate, and J. C. Fuggle, *Phys. Rev. B,* **48** 2074 (1993).

[79] R. Ruus, A. Kikas, A. Saar, A. Ausmees, E. Nommiste, J. Aaik, A. Aidla, T. Uustare, and I. Martinson, *Solid State Commun.*, **104**, 199 (1997).

[80] M. F. Ruiz-Lopez and A. Munoz-Paez, *J. Phys: Condens. Matter*, **3**, 8981 (1991).

[81] D. W. Fischer, *Phys. Rev. B*, **5**, 4219 (1972).

[82] K. Fan, M. Liu, T. Peng, L. Ma, K. Dai, *Renewable Energy*, **35**, 555 (2010).

[83] R. Brodson, B. G. Williams, W. Engle, H. Sauer, E. Zeitler, and J. M. Thomas, *Solid State Commun.*, **64** ,609 (1987).

[84] L. Soriano, M. Abbate, J. Vogel, J. C. Fuggle, A. Fernández, A. R. González-Ehpe, M. Sacchi, and J. M. Sanz, *Surf. Sci.*, **290**, 427 (1993).

[85] J. Biener, M. Bäumer, J. Wang, and R. J. Madix, *Surf. Sci.*, **450**, 12 (2000).

[86] J. P. Crocombette and F. J. Jollet, *J. Phys. Condens. Matter*, **6**, 10811 (1994).

[87] L. A. Grunes and R. D. Leapman, *J. Phys. Rev. B*, **25**, 7157 (1982).

[88] E. Z. Kurmaev, R. G. Wilks, R. Filby, A. Moewes, L. Müller, and F. A. Müller, *Mater. Sci. Eng. C*, **29**, 136 (2009).

[89] J. Biener, M. Baumer, and R. J. Madix, *Surf. Sci.*, **432**, 178 (1999).

[90] K. S. Raja, T. Gandhi, M. Misra, *Electrochem. Commun.*, **9**, 1069 (2007).

[91] D. Chen, Z. Jiang, J. Geng, J. Zhu, and D. Yang, *J. Nanopart Res*., **11**, 303 (2009).

[92] O. V. Overschelde, S. Dinu, G. Guisbiers, F. Monteverde, C. Nouvellon, and M. Wautelet, *Appl. Surf. Sci.*, **252**, 4722 (2006).

[93] S. Kitazawa , Y. Choi, S. Yamamoto, and T. Yamaki, *Thin Solid Films*, **515**, 1901 (2006).

[94] O. V. Overschelde, J. M. Boisdequin, Ph. Leclère, and M. Wautelet, *Phys. Status Solidi C*, **10**, 3255 (2008).

[95] J. Kim, J. Kim, and M. Lee, *Nanotechnology*, **21**, 345203 (2010).

[96] V. Stengl, S. Bakardjieva, J. Subrt, and L. Szatmary, *Microporous Mesoporous Mater.*, **91**, 1 (2006).

[97] S. J. Rhee, S. Kim, C. W. Sterner, J. O. White, and S. G. Bishop, *J. Appl. Phys.*, **90**, 2760 (2001).

[98] M. W. Ha, S. C. Lee, J. H. Park, K. S. Seo, and M. K. Han, *Phys. Scr.*, **T126**, 27 (2006).

[99] L. Guo, J.Wang, Z. Lin, S. Gacek, and X. Wang, *J. Appl. Phys.*, **106**, 123526 (2009).

[100] G. Foti, E. Rimini, and S. U. Campisano, *Phys. Status Solidi A*, **47**, 533 (1978).

[101] S. Bauer, S. Kleber, and P. Schmuki, *Electrochem. Commun.*, **8**, 1321 (2006).

[102] I. Paramasivam, J.M. Macak, T. Selvam, and P. Schmuki, *Electrochim. Acta*, **54**, 643 (2008).

[103] Y. Yang, X. Wang, and L. Li, *J. Am. Ceram. Soc.*, **91**, 3086 (2008).

[104] L. Sun, S. Zhang, X.W. Sun, and X. He, *J. Electroanal. Chem.*,**637**, 6 (2009).

[105] H. Yin, H. Liu, and W.Z. Shen, *Nanotechnology*, **21**, 035601 (2010).

[106] H. Liu, L. Tao, and W. Shen, *Nanotechnology*, **22**, 155603 (2011).

[107] S. D. Sharma, K. K. Saini, C. Kant, C. P. Sharma, S. C. *Jain, Appl. Catal. B*, **84**, 233 (2008).

[108] S. Brunauer, P. H. Emmett, and E. Teller, *J. Am. Chem. Soc.*, **60**, 309 (1938).

[109] D.S. Kima and S.Y. Kwak, *Appl. Catal. A*, **323**, 110 (2007).

Vita

【Personal information】

Name: 徐明義 / Ming-Yi Hsu

Gender: Male

Date of birth: 1981/11/04

Nationality: Taiwan (R.O.C)

E-mail: vincent.mse95g@nctu.edu.tw

【Education】

Degree	Name of School / Major	From	To	Research Advisor
Ph.D	National Chiao Tung University Materials Science and Engineering	Sep. 2006	May 2012	Jihperng Leu
MS	Feng Chia University Materials Science and Engineering	Sep. 2004	Jun. 2006	Ju-Liang He ; Keh-Chang Chen
BS	Feng Chia University Materials Science and Engineering	Sep. 2000	Jun. 2004	

【Experience】

➢ **Instrumental assistant:**

- Laser scattering particle size distribution analyzer in dept. of NCTU (2006-2010)
- BET surface area analyzer in dept. of NCTU (2006-2010)

➢ **Teaching assistant:**

- Introduction to materials science in dept. of NCTU (2007)
- VLSI manufacture technology in dept. of NCTU (2008)
- Introduction of crystallography and diffraction in dept. of NCTU (2009)
- Low-k materials and processing technologies in dept. of NCTU (2009)

【Theses】

> **Master degree**

模板式生長二氧化鈦奈米管之染料敏化太陽能電池研究

Titanium Dioxide Nano-tubes Growth via Template for Dye-sensitized Solar Cell

> **Ph.D degree**

二氧化鈦奈米管陣列與複合結構之形貌與結構特性及其光催化性質之研究

Morphological and Microstructural Study on TiO_2 Nanotube Arrays and Hybrid Structure and Their Photocatalytic Performance

【Publications】

> **Journal papers**

- **Ming-Yi Hsu**, Nguyen Van Thang, Chih Wang, and Jihperng Leu, Structural and morphological transformations of TiO_2 nanotube arrays induced by excimer laser treatment, Thin Solid Films, 520 (2012) 3593-3599.

- **Ming-Yi Hsu**, Wei-Chun Yang, Hsisheng Teng, and Jihperng Leu, Microstructure and composition of TiO_2 nanotube arrays fabricated with HF and NH_4F electrolytes and their evolution during annealing, Journal of The Electrochemical Society, Vol.158, No.3, K81-K87 (2011).

- 何主亮、**徐明義**、李幸芳、陳炯勳,"納米線/模板共構染料敏化二氧化鈦太陽電池的製備," 過程工程學報 (EI), 6/SUPPL. 2, PP. 228~234, 2006-12. (EI)

- 何主亮、陳炯勳、**徐明義**、陳克昌,"液相沉積奈米 TiO_2 薄膜及後熱處理對染料敏化太陽能電池之影響," 過程工程學報 (EI), 6/SUPPL. 2, PP. 224~227, 2006-12. (EI)

> **Conference papers**

- Van Thang Nguyen, **Ming-Yi Hsu**, Chih Wang, and Jihperng Leu, "Structural transformation of titania nanotube arrays induced by excimer laser annealing," 2010 Materials Research Society Taiwan, November 19~20, 2010, I Shou University, Dashu, Kaohsiung, Taiwan.

- Wan-Ting Hsu, **Ming-Yi Hsu**, Hsin-Lin Hsu, and Jihperng Leu, "Tailoring the pore morphology of mesoporous TiO_2 films using PEG for dye-sensitized solar cells," 2010 Materials Research Society Taiwan, November 19~20, 2010, I Shou University, Dashu, Kaohsiung, Taiwan.

- **Ming-Yi Hsu**, Harold Liao, Wei-Chun Yang, and Jihperng Leu, "Microstructures and formation mechanism of the self-organized growth TiO_2 nanotube arrays by anodic oxidation",中國材料科學學會 2008 年年會論文集,P01-166 能源與環保材料, 2008 年 11 月 21-22 日,台灣 台北。

- T. H. Chiu, J.T. Chang, **M. Y. Hsu**, A. Davison, "An Attempt to Prepare TiO_2 Layer for Dye-Sensitized Solar Cell by Using Arc Ion Plating," Renewable Energy 2006 , P365-368, 2006-10. Makuhari, Chiba, Japan.

- 陳炯勳、**徐明義**、陳克昌、何主亮,"液相沉積奈米 TiO_2 薄膜及後熱處理對染料敏化太陽能電池之影響," 中國顆粒學會 2006 年年會暨海峽兩岸顆粒技術研討會,論文集,P276-279 , 2006-08. 中國北京.

- **徐明義**、李幸芳、陳炯勳、何主亮,"奈米線/範本共構之染料敏化二氧化鈦太陽電池," 中國顆粒學會 2006 年年會暨海峽兩岸顆粒技術研討會, 論文集,P280-285 , 2006-08,中國北京.

- 李幸芳、**徐明義**、陳炯勳、林繼榮、陳克昌、何主亮,"微弧氧化生長二氧化鈦應用於反向結構太陽能電池之嘗試," 2006 海峽兩案奈米材料技術研討會, A037P, P33 , 2006-04, 台北大同大學.

- 陳炯勳、**徐明義**、何主亮、陳克昌,"利用液相沉積法製備奈米二氧化鈦薄膜應用於染料敏化太陽能電池," 2006 海峽兩案奈米材料技術研討會 , A038P, P34 , 2006-04, 台北大同大學.

- 陳炯勳、**徐明義**、何主亮、陳克昌,"利用液相沉積法製備奈米 TiO_2 薄膜應用於染料敏化太陽能電池," 2005 台灣鍍膜科技協會薄膜與奈米科技研討會暨國科會專題計畫研究成果發表, 45 , 2005-12, 日月潭.